Chapter 6

OXIDE SEMICONDUCTORS: SUSPENDED NANOPARTICLE SYSTEMS

6.1 Introduction

Our discussions to this point on the use of semiconductor materials for photo-assisted water splitting have been predicated on the use on a clearly defined anode and cathode geometry as initially described by Fujishima and Honda [1] where the hydrogen and oxygen are evolved separately. While this approach offers the fundamental advantage that no gas separation step is required, the photoconversion efficiency suffers from losses inherent in the transport of the photogenerated electrons and H^+ ions from the anode to the cathode. In variations on a water-splitting theme, in 1977 Schrauzer and Guth used a TiO_2-based photocatalyst to carry out the photocatalytic decomposition of water vapor under UV light [2], resulting in the simultaneous co-generation of oxygen and hydrogen. Subsequent efforts investigated the use of various doped TiO_2 surfaces for direct photocatalytic splitting of water vapor [2-5] with the mixed evolution of hydrogen and oxygen. Effectively, rather than an electrode-based electrochemical cell each semiconductor particle can behave as its own electrochemical cell, see **Fig. 6.1**, being considered as a micro-homogenous or micro-heterogeneous system. The logical extension of this idea, bulk to planar to particulate, is a dispersion of semiconductor nano 'particles' of various geometry, e.g. sphere, tube, ribbon, or wire, see **Fig. 6.2**, throughout either liquid or vapor phase water resulting in the photocatalytic splitting thereof. The concept offers an appealing simplicity that has gained considerable academic interest.

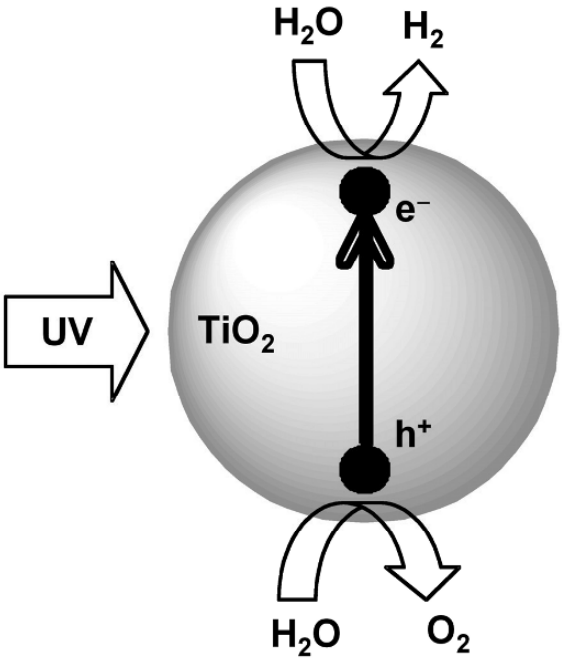

Fig. 6.1: A schematic drawing of a semiconductor particle behaving as its own electrochemical cell for water splitting.

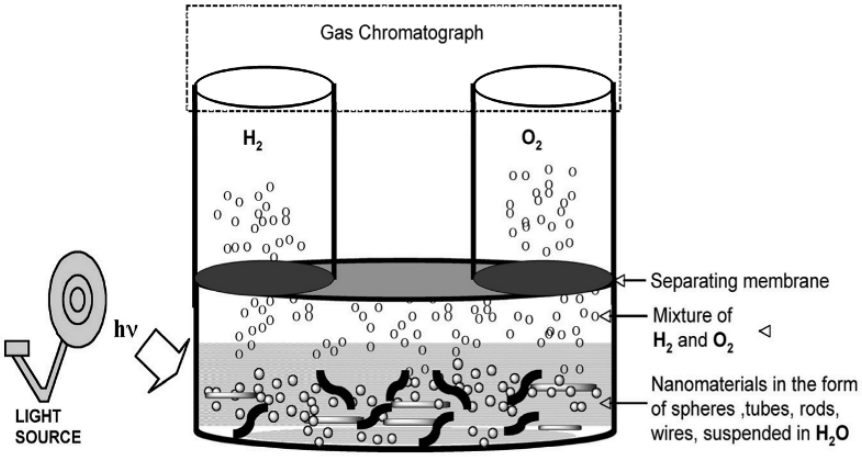

Fig. 6.2: A schematic diagram showing suspended nanomaterials in the form of spheres, rods, tubes or wires dispersed throughout some water. Under solar light illumination, hydrogen and oxygen evolved from these small particles. A membrane is placed atop the reaction vessel to separate H_2 and O_2.

Several modified TiO_2 catalysts in powder form, including Pt-TiO_2, Pt-RuO_2-TiO_2, Pt-$SrTiO_3$, NiO-$SrTiO_3$, suspended or dispersed in liquid water for solar hydrogen production have been studied [6-18]. To date no homogeneous or heterogeneous photocatalysts have been found suitable for stoichiometric water splitting, primarily due to the difficulty in oxygen formation and the rapid reverse reaction between products. Of the reported studies [6-18], efforts have focused on approaches such as metal loading, ion doping, composite formation, and the addition of electron donors or hole scavengers with an aim towards preventing the rapid recombination of photogenerated electron/hole pairs, and improving the visible light response of the semiconducting particles. As we will discuss further, these photocatalysts involve a two-step water splitting process for H_2 production and are comprised of a combination of either metal and/or two or more different oxide semiconductors. Modification of these nanoparticle photocatalysts has resulted in comparatively effective catalysts for H_2 evolution [19-26]. The high surface area of these nanoparticles, at least in principle, allow solution species to capture photogenerated electrons quickly and thereby significantly reduce the occurrence of charge recombination [25-27].

Over the past several years considerable effort has been made to design, synthesize and fabricate metal oxide nanoparticle photocatalysts capable of using visible light energy. Cu_2O, which behaves as a p-type semiconductor with a band gap energy of 2.0-2.2 eV, was the first such oxide reported for decomposing water under visible light irradiation [28]. The release of excess O_2 from Cu_2O by visible light irradiation disturbs the water splitting stoichiometry due to photoadsorption of oxygen in the bulk, and O^- and O_2^- at the surface of Cu_2O. Since the photoadsorption largely depends on the O_2 pressure as well as on the wavelength and intensity of light, at modest pressures (above ≈ 500 Pa) photoadsorption inhibits water splitting on Cu_2O [28]. Anion doping of wide band gap semiconductors has been an area of particular recent interest [29,30], but a robust design has yet to be realized. Several review articles [24-26,31-33] consider the importance of semiconductor particulate systems for solar hydrogen production.

Nanoparticles are usually defined as particles having one or more dimensions on the order of 100 nm or less. Nanoparticles of approximately 10 nm diameter are variously labeled as quantum dots, demonstrating size-dependent quantization of the electronic energy levels as dependent upon particle size and shape, particle-particle spacing, and nature of the outer shell. The interesting and sometimes unexpected nanoparticle properties are partly due to aspects of the material surface dominating those of the bulk. The large fraction of atoms at the surface of a material becomes significant as the size of that material approaches the nanoscale. For example, the interaction between the nanoparticle surface and a surrounding liquid is commonly strong enough to overcome differences in density, allowing it to form a suspension rather than sinking or floating. Nanoparticle synthesis methods play an important role in determining the specificity of the various properties, including physical properties and those of the electronic structure, e.g. quantum confinements and electron tunneling.

6.2 Nanoparticle-Based Photocatalytic Water Splitting

The following reactions are involved for the production of hydrogen and oxygen from water (pH = 7):

$$2H_2O + 2e^- \rightarrow H_2 + 2OH^-, \quad E°(H_2/H_2O) = -0.41 \text{ V (vs NHE)} \qquad (6.2.1)$$

$$2H_2O \rightarrow O_2 + 4H^+ + 4e^-, \quad E°(H_2O/O_2) = +0.82 \text{ V (vs NHE)} \qquad (6.2.2)$$

$$E°_{overall} = E°(H_2O/O_2) - E°(H_2/H_2O) = 1.23 \text{ V}$$

The reaction

$$H_2O \rightarrow H_2 + 1/2O_2$$

is endothermic and involves a change in the Gibbs free energy ($\Delta G°$ = 2.46 eV or 237.2 KJ mol^{-1}). The overall reaction is a 2-electron redox process. The energy of 1.23 eV per electron transferred corresponds to a wavelength of λ = 1008 nm. Water absorbs solar radiation in the infrared region, with photon energies too low to drive photochemical water splitting. Thus any photochemical

process to drive the water splitting reaction must involve a sensitizer or semiconductor that can absorb light. Semiconductors, in the presence of energy provided by light, are capable of decomposing water into hydrogen and oxygen depending upon their conduction band (CB) and valance band (VB) energy levels. The conduction band level should be more negative than the hydrogen evolution level, $E°(H_2/H_2O)$, while the valance band level should be more positive than the water oxidation level, $E°(H_2O/O_2)$.

When a semiconductor is irradiated by photons of energy equal to or greater than that of its bandgap, which it absorbs, excitation occurs and an electron moves to the conduction band leaving a hole behind in the valance band. For TiO_2 this process is expressed as:

Semiconductor: $$TiO_2 + h\nu \rightarrow e^-(TiO_2) + h^+(TiO_2) \quad (6.2.3)$$

Water: $$H_2O \rightarrow H^+ + OH^- \quad (6.2.4)$$

$$2e^-(TiO_2) + 2H^+ \rightarrow H_2 \quad (6.2.5)$$

$$2h^+(TiO_2) + 2OH^- \rightarrow 2H^+ + 1/2O_2 \quad (6.2.6)$$

The photogenerated electrons and holes can recombine in bulk or on the semiconductor surface releasing energy in the form of heat or a photon. The electrons and holes that migrate to the semiconductor surface without recombination can, respectively, reduce and oxidize water (or the reactant) and are the basic mechanism of photocatalytic hydrogen production, see **Fig. 6.3.**

The efficiency of converting light energy into hydrogen energy using suspended nanoparticle catalysts is, to date, low. The primary reasons for the low efficiencies are: {**1**} Rapid recombination of photo-generated electron-hole pairs. {**2**} Photochemical water-splitting involves at least one exthothermic reaction therefore it is relatively easy for molecular hydrogen and oxygen to recombine (backward reaction).

$$H_2(g) + 1/2O_2(g) \rightarrow H_2O(g) + 57\ Kcal \quad (6.2.7)$$

{**3**} The poor visible spectrum response of corrosion resistant catalysts. For example TiO_2, which is one of the most suitable

photocatalysts being chemically stable with strong catalytic activity, does not respond to visible light.

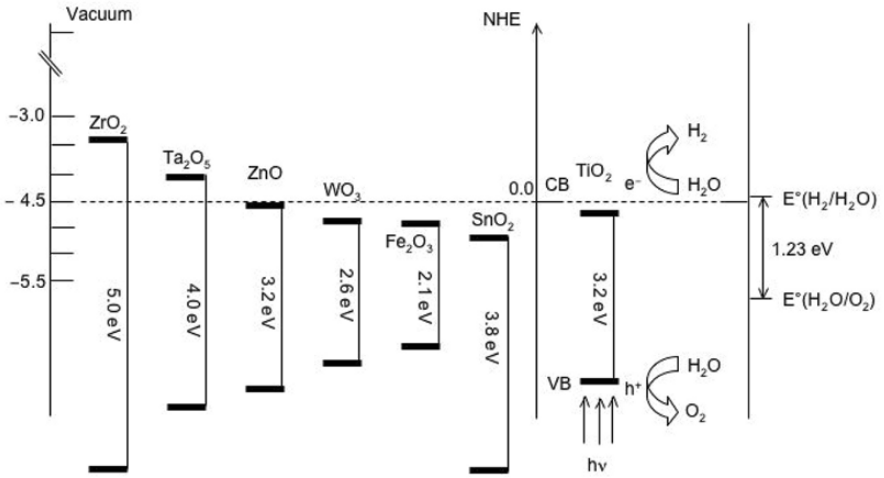

Fig. 6.3: Band position of several semiconductors in presence of aqueous electrolyte at pH = 1. Energy scale is indicated in electron volts (eV) using either normal hydrogen electrode or vacuum level as a reference. On right energy levels for TiO_2 photocatalytic water splitting are presented.

A significant enhancement in photocatalytic activities have been found in particles less than 10-15 nm in diameter, a behavior attributed to quantum size effects. Photochemical reactions at the semiconductor surface occur if the light-generated charge carriers reach the surface finding suitable reaction partners, protons for electrons and donor molecules for holes. For small particles, the charge carrier diffusion length is large compared to the particle size and no internal electric field (depletion layer) is necessary to separate the photogenerated electron-hole pairs. Therefore, the probability that the charge carriers will reach the surface of the particle increases as the particle size decreases.

6.3 Nanoparticle Synthesis Techniques

There are various methods available for the synthesis of 1-100 nm diameter nanoparticles. Whatever the synthesis method, it is important to consider their stability in terms of composition and size.

The surface atoms of a nanoparticle may be quite active and tend to react in the ambient environment. Smaller particles may tend to coagulate to form larger particles losing their interesting size dependent properties. Therefore synthesis methods that passivate the particles to ensure their long-term stability have gained significant interest. Liquid-phase nanoparticle synthesis routes typically yield non-aggregating nanoparticles with uniform size and shape and controlled surface properties; such desirable properties are difficult to achieve using gas-phase synthesis routes. However in contrast to liquid phase methods, gas-phase methods have been scaled for large-scale production of specific nanoparticle compositions. A few commonly used methods for metal oxide nanoparticle synthesis are shown in **Fig. 6.4**. We now briefly consider some nanoparticle synthesis routes; more detailed synthesis techniques are suggested to the reader for liquid phase [34-35] and gas phase [36-37].

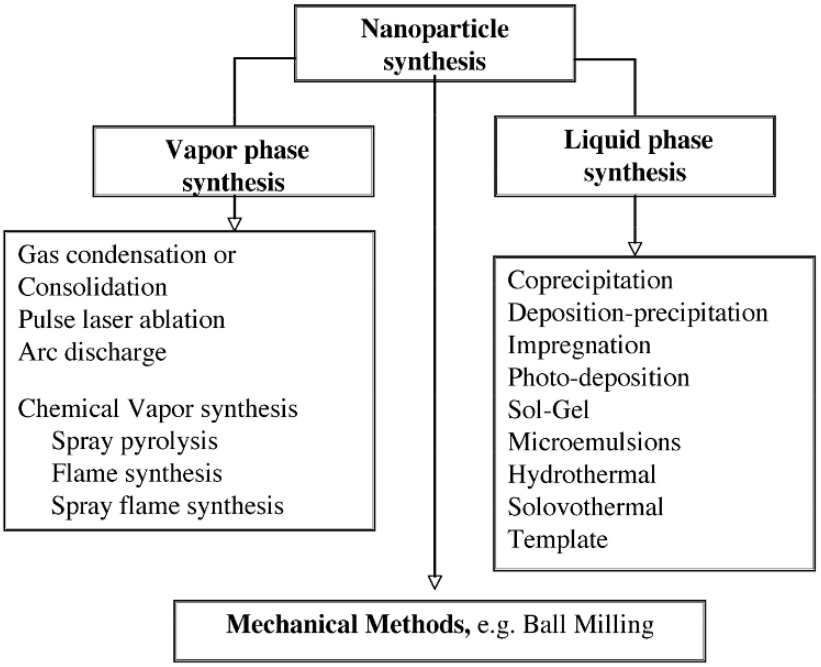

Fig. 6.4: Flow chart illustrating various nanoparticle synthesis routes.

6.3.1 Liquid-Phase Nanoparticle Synthesis

Coprecipitation [38-42]

The simultaneous occurrence of nucleation, growth, coarsening (Ostwald ripening), and agglomeration are key features of coprecipitation reactions. This method involves the simultaneous precipitation of insoluble compounds in a solution coming out from mixed, and well-defined, quantities of different ionic solutions under controlled reaction conditions. A variety of metal oxide nanoparticle compositions, and metal nanoparticles supported on metal oxides, can be prepared by the coprecipitation of sparingly soluble compounds followed by their calcination to oxide form [38-40]. The mechanistic pathways of coprecipitation processes are still unclear because of the difficulties in isolating and then studying each process separately. It is understood that a state of high supersaturation of sparingly soluble compounds in an aqueous solution dictates the key nucleation step in the precipitation process, thereby forming a large number of small particles. Coarsening and aggregation processes usually determine the morphology and size distribution of resulting particles. Agglomeration of small metal particles is inevitable in the absence of any stabilizers. Steric stabilization and colloid stabilization are the two appropriate choices concerning the chemical stability of monodispersed nanoparticles at very high or very low pH. Some agglomeration appears unavoidable in the precipitation reaction of oxides where annealing or calcination is usually required.

For mixed metal oxides obtained from their hydroxide or carbonate precursors after calcination, it is generally difficult to determine whether the as-prepared precursor is a single-phase or multiphase solid solution [35]. Non-aqueous solvents appear superior for achieving two dissimilar metal oxides such as $MM'O_2$ or $MM'O_4$ precipitates; such reactions cannot be carried out simultaneously in aqueous solution due to the large variations in pH necessary to induce precipitations [41,42]. **Table 6.1** summarizes some of the nanoparticulate semiconducting metal oxides and mixed metal oxides prepared via co-precipitation techniques. The general procedure of achieving metal loaded nanoparticles on an oxide support is shown in **Fig.6.5.**

Table 6.1 Summary of the reactions for the synthesis of oxides nanoparticle by different methods

Compounds	Starting Materials	Precipitation agent	Stabilizer	Chelating agent	Polymerizing agaent	Conditions (°C)	Product size (nm)	Ref.
Coprecipitation								
NiO	$NiCl_2$	NH_4OH	CTAB			500	22-28	38
ZnO	ZnC_2	NH_4OH	CTAB			500	40-60	38
SnO_2	$SnCl_4$	NH_4OH	CTAB			500	11-18	38
Sb_2O_3	$SbCl_3$	NaOH	PVA			350	10-80	39
Au/Fe_2O_3	$HAuCl_4$ $Fe(NO_3)_3$	Na_2CO_3	-			400	3.6	40
Fe_3O_4	$FeCl_2$, $FeCl_3$	NH_4OH	H^+			N_2 atm	8-50	41
$MnFe_2O_4$	$MnCl_2$, $FeCl_3$	$N_2H_4.H_2O$	None			500	5-25	42
Sol-gel								
$ZnTiO_3$	$Zn(OAc)_2$, $Ti(^tOBu)_4$			CA	EG	500-1000	18-31	53
$SrTiO_3$	$Sr(NO_3)_2$, $Ti(^tOBu)_4$			GAA	PT	750	12-25	54
$BaTi_4O_9$	$Ba(OAc)_2$, $Ti(^IOpr)_4$					600-1000	Not stated	55
$La_2Ti_2O_7$	$Ti(^IOBu)_4$, $La(NO_3)_2$			CA	EG	650-1150	55	56
$Sr_2Nb_xTa_{2-x}O_7$	$NbCl_5$, $TaCl_5$, $SrCO_3$			CA	EG	700-1000	Not stated	57

CTAB: Cetyltrimethylammonium bromide; PVA: Polyvinyl alcohol; CA: Citric Acid; EG: Ethylene Glycol; PAA: Polyacrylic acid; GAA: Glacial Acetic Acid; PT; Propanetriol

Deposition-Precipitation [40,43-45]

A modified version of a simultaneous precipitation reaction, this is a highly selective approach for generating noble metal nanoparticles on metal oxide supports, see **Fig. 6.5**. The nanoparticle size can be controlled by adjusting the reaction pH. Pt, Au, Ag nanoparticles can be deposited on a variety of metal oxide supports such as TiO_2, Fe_2O_3, and ZnO.

Photo-deposition [17,45-48]

This similar methods involves UV light irradiation, with light intensity, stirring speed, suspension volume and temperature influencing particle growth, **Fig. 6.5.** Shorter irradiation times can be used to limit the amount of particle deposition. Photo-deposited samples do not require calcination hence there is little chance of particle agglomeration.

Impregnation [13,45,49,50]

This method involves the repeated dipping of porous support materials into a solution containing the desired catalytic agent. It is then dried and calcined to transform the metal into insoluble form. The agent must be applied uniformly in a predetermined quantity to a preset depth of penetration. The metal loading in the finished catalyst is typically 1-5%, **Fig. 6.5.**

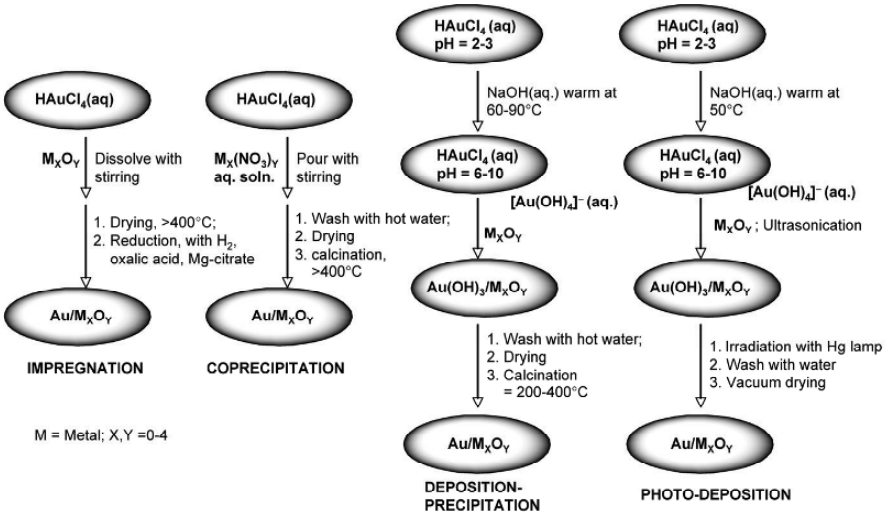

Fig. 6.5: Syntheses of metal loaded nanoparticles (Au) on metal oxide supports using impregnation, coprecipitation, deposition-precipitation, and photo-deposition methods. For Pt loaded nanoparticles H_2PtCl_6 (aq) is used.

Sol-gel Processes [51-57]

The sol is made of a stable suspended solution of metal salts or solvated metal precursors containing solid particles of nanometer diameter. Polycondensation or polyesterification results in the appearance of particles in a new phase called “the gel”. Aging, drying and dehydration are steps required to achieve solid-form ultra-fine particles. Coarsening and phase transformation occur simultaneously with aging. Gel drying is associated with the

removal of water or other volatile liquids from the gel network, either by thermal evaporation or near supercritical condition resulting in a monolithic structure called, respectively, a xerogel or an aerogel. Dehydration, typically by calcination, removes surface bound hydroxy functional groups. This method is ideally suited for generating metal oxide nanoparticles.

Calcining aerogels or xerogels improves sample crystallinity but normally leads to partial agglomeration. For example, condensation and supercritical drying of $Zr(NO_3)_2 \cdot 5H_2O$ or $Zr(NO_3)_2 \cdot 2H_2O$ precursors in alcohol yield amorphous ZrO_2 nanoparticles (~ 1 nm), which upon calcination at 400°C form 2-3 nm-agglomerated nanoparticles in crystalline form [51]. Similarly, TiO_2 nanoparticles can be prepared by controlled hydrolysis and condensation of $Ti(OPr)_4$ in an alcohol + HCl solution followed by supercritical drying [52].

A modified sol-gel process developed by Pechini [53] provides easy synthesis of mixed metal oxides of considerable complexity. In this method, chelating agents tend to form stable complexes with a variety of metals over fairly wide range of pH. Selective synthesis techniques are presented in **Table 6.1**. However because of the formation of gel network by the polyesterification of the chelating and polymerization agents, in which metal ions remain trapped in their matrices, this method provides limited control over particle size, shape and morphology. Synthesis of $ZnTiO_3$ is one such example where citric acid and ethylene glycol act, respectively, as chelating and polymerization agents, thus forming ≈ 30 nm particles from $Zn(OAc)_2$ and $Ti(OBu)_4$ as starting materials [53].

Microemulsion Methods [58-59]

This method involves formation of reverse micelles in the presence of surfactants at a water-oil interface. A clear homogeneous solution obtained by the addition of another amine or alcohol-based co-surfactant is termed a Microemulsion. To a reverse micelle solution containing a dissolved metal salt, a second reverse micelle solution containing a suitable reducing agent is added reducing the metal cations to metals. The synthesis of oxides from reverse micelles depends on the coprecipitation of one or more metal ions from

aqueous solution. This method is similar to coprecipitation, and is useful in preparing 20-80 nm diameter ferrite nanoparticles, MFe_2O_4 [M = Fe, Mn, Co] [58]. For insoluble or unstable metal ions, nanoparticles can be prepared by the hydrolysis of a suitable precursor in common with sol-gel. Synthesis of mesoporous mixed zirconium-titanium phosphates (~50 nm particles) using cationic surfactants, octadecyltrimethylammonium chloride, has successfully demonstrated water decomposition [59].

Solvothermal/Hydrothermal Methods [60-65]

Within a sealed vessel such as an autoclave the reaction temperature of a medium can be brought to well above its boiling point by an increase in the self-generating pressure with heating. The solvothermal method is similar to the hydrothermal method except that organic solvents are used instead of water. This method can effectively prevent the product from oxidizing and has been used to synthesize a variety of non-oxide compositions. Some of these reactions involve supercritical solvents, and thus take advantage of the increased solubility and reactivity of inorganic salts at elevated temperatures and pressures. Due to the high viscosities of supercritical solvents various chemical compounds are readily dissolved that would, under ambient conditions, remain insoluble. Both these processes have advantages over coprecipitation and sol-gel, because the reaction products are usually crystalline. For example, hydrothermal synthesis of monodispersed, anatase/rutile nanocrystalline TiO_2 particles has been successfully carried out [60], as well as preparation of metal-doped titania particles [61,62]. Codoping with bromine and chlorine under hydrothermal conditions yields titania of mixed anatase/rutile phase which has shown water splitting in Na_2CO_3 under UV light irradiation [63]. Nanocrystalline TiO_2 photocatalysts of controllable anatase/rutile ratio and high surface area (113-169 m^2/g) have been prepared at low temperature by a microemulsion-mediated hydrothermal method [64]. Water splitting by NiO doped, hydrothermally synthesized pyrochlores of tantalates ($Ca_2Ta_2O_7$, $Na_2Ta_2O_6$) is reported by Ikeda and co-workers [65].

Template Methods [66-69]

Various metal and metal oxide nanoparticles have been prepared on polymer (sacrificial) templates, with the polymers subsequently removed. Synthesis of nanoparticles inside mesoporus materials such as MCM-41 is an illustrative template synthesis route. In this method, ions adsorbed into the pores can subsequently be oxidized or reduced to nanoparticulate materials (oxides or metals). Such composite materials are particularly attractive as supported catalysts. A classical example of the technique is deposition of 10 nm particles of NiO inside the pore structure of MCM-41 by impregnating the mesoporus material with an aqueous solution of nickel citrate followed by calicination of the composite at 450°C in air [68]. Successful synthesis of nanosized perovskites (ABO_3) and spinels (AB_2O_4), such as $LaMnO_3$ and $CuMn_2O_4$, of high surface area have been demonstrated using a porous silica template [69].

6.3.2 Vapor Phase Nanoparticle Synthesis

Within this method nanoparticle production can be divided into gas-to-particle and liquid/solid-to-solid routes. In the liquid/solid-to-solid route the product particles are formed from droplets or solid reactant particles via intraparticle reactions. Using this method it is possible to produce single- and multi-component materials with controlled levels of doping, however multi-component materials may be difficult to produce. In the gas-to-particle route, the most essential requirement is to create a high degree of vapor supersaturation of the source materials. Supersaturation can be achieved via physical processes such as cooling of a hot vapor or via chemical reactions of gaseous precursors, which results in the formation of condensable species. Under favorable conditions nucleation and particle growth occur that are controllable either by changing the reaction parameters or by removing the source materials. Once the particles form in the gas phase, coagulation and coalescence assume significant importance. Solid, spherical or nearly spherical particles with narrow size distributions can be produced of high purity. However in contrast to liquid phase where capping with appropriate ligand can be used to stabilize a nanoparticle dispersion, special efforts are needed to control agglomeration.

Chemical Vapor Synthesis [70-74]

Similar to chemical vapor deposition, reactants or precursors for chemical vapor synthesis are volatile metal-organics, carbonyls, hydrides, chlorides, etc. delivered to the hot-wall reactor as a vapor. A typical laboratory reactor consists of a precursor delivery system, a reaction zone, a particle collector, and a pumping system. Modification of the precursor delivery system and the reaction zone allows synthesis of pure oxide, doped oxide, or multi-component nanoparticles. For example, copper nanoparticles can be prepared from copper acetylacetone complexes [70], while europium doped yttiria can be obtained from their organometallic precursors [71].

Instead of delivering the reactant into a hot wall furnace it can be injected using a nebulizer, a technique referred to as spray pyrolysis [72]. Flame synthesis is widely used for nanoparticle production due to its cost-effectiveness and versatile approach for controlled synthesis. In a flame reactor, the energy from the flame drives the chemical reactions producing clusters, which subsequently grow into nanoparticles by surface growth and /or coagulation and coalescence at elevated temperature [73]. Flame spray pyrolysis uses low vapor-pressure liquid precursors, with evaporation and ignition of the spray (liquid removal) initiated by a flame ring about the nozzle. Subsequent gas phase reaction followed by vapor condensation leads to the growth of the nanoscale particles [74].

Gas condensation [75-79]

This method involves a means of achieving supersaturation by heating solid precursors directly into vapor. The gas so produced, when passed through a cold stream of inert gas, condenses in the form of small nanocrystalline metal particles. Metal-oxides can be obtained by including O_2 in the inert gas stream. Composite materials can be achieved by mixing two or more evaporation sources. The particle size distribution is controlled through the evaporation and condensation rates [75,76]. One variation of this method is arc discharge [37,77], where metal electrodes are vaporized under high voltage acceleration. Alternatively laser ablation [78,79] can be used for generating nanoparticles of high melting point compounds.

6.3.3 Mechanical Methods of Nanoparticle Synthesis [80-81]

Grinding and mixing of powder samples with or without liquid in a rotating mill partly filled with grinding media such as balls or pebbles can be used to reduce particle sizes to the nanometer range. Magnetic and catalytic nanoparticles can usually be produced by this method. Although a simple technique of relatively low cost it produces particles of broad size distribution, while contamination from the milling equipment is often a problem.

6.4 Synthesis of Complex Oxide Semiconductors

Most of the oxide semiconductors synthesized for H_2 production from aqueous suspension are composed of two or more components, hence the design and preparation of efficient photocatalyst materials are of paramount importance. For example, in the presence of NiO $SrTiO_3$ (perovskite type) is a highly active catalyst for water decomposition. Barium tetratitanate $BaTi_4O_9$, acts as an excellent catalyst when combined with RuO_2. Ruddlesden-Popper-type hydrous layered perovskites, $H_2La_{2/3}Ta_2O_7$, have shown higher activity than anhydrous perovskites ($KTaO_3$, $La_{1/3}TaO_3$) for photocatalytic water splitting under UV irradiation [82], while intercalation of Ni cocatalyst to $H_2La_{2/3}Ta_2O_7$ via an ion-exchange reaction further increases the activity. The photocatalytic activity of Dion-Jacobson-type layered perovskite, $K[Ca_2Nb_3O_{10}]$, is significantly enhanced by Pt loading [83]. The layered oxide was exfoliated into unilamellar nanosheets, which were subsequently loaded with Pt nanoparticles via photodeposition. The Pt-loaded nanosheets were flocculated with alkali-metal ions to restore a layered aggregate. Through this route Pt nanoparticles can be incorporated in a highly dispersed fashion into the host lattice of the layered perovskite [83]. Overall water splitting is observed with RuO_x-loaded $A[Ca_2Nb_3O_{10}]$ ($A = LI^+$, Na^+, K^+) restacked perovskite nanosheets under UV light irradiation [84]. It is clear from these examples that there are advantages in using a heterogeneous "oxide semiconductor system" consisting of two or more active components. To fabricate such a system requires, in general, multiple synthesis steps with impregnation and photodeposition the two most widely used methods for loading of the co-catalysts.

The majority of perovskite or layered perovskite type materials based on Nb(V), Ta(V) and Ti(IV) involve conventional solid-state reaction preparative methods, in which appropriate amounts of precursor oxides or carbonates are ground together and then calcined at high temperatures (typically 1000-1300°C) for times sufficient to allow cation interdiffusion. The materials produced by this method have low surface area, uncontrolled grain growth, localized segregation of the components, and possible loss of stoichiometry due to volatilization of the constituent components. To a great extent these underlying issues decrease the photocatalytic activity of a given catalyst. The Pechini-type sol-gel process (polymerizable complex) based on polyesterification between citric acid and ethylene glycol provides a better alternate strategy to synthesize mixed metal oxides, such as $M_xM'_yM''_zO_7$ (x, y, z = 0-4; M, M′, and M″ represent three different metals), which yield ultra-fine nanoscale particles [56, 57]. **Figure 6.6** shows a flow chart of the synthesis procedure for $La_2Ti_2O_7$ crystals by the polymerizable complex method.

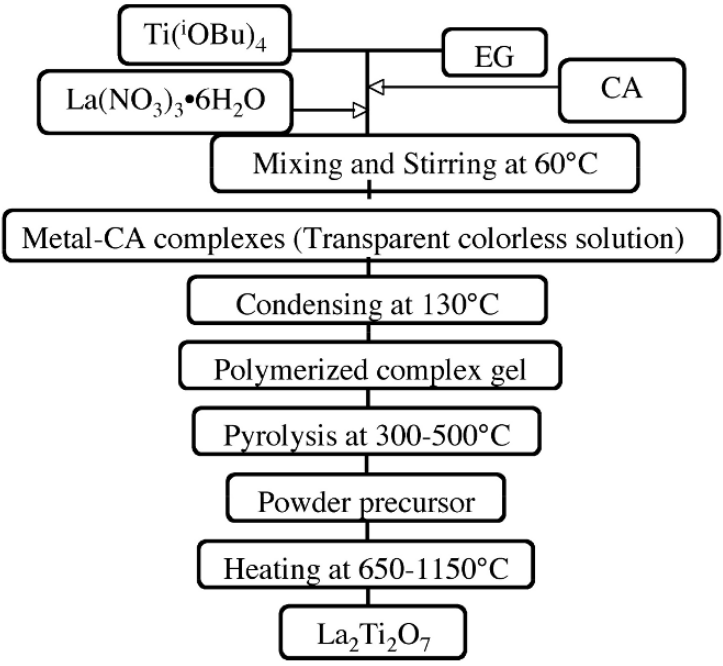

Fig. 6.6: A flow-chart for preparing $La_2Ti_2O_7$ by the Pechini-type sol-gel (polymerizable complex) method [56].

Metal, metal oxide, and mixed-metal oxide nanoparticles are strongly affected by heat treatments that lead to particle agglomeration, with a corresponding reduction in photocatalytic activities. Visible-light active zinc ferrite doped titania, TiO_2-$ZnFe_2O_4$ photocatalysts prepared by sol-gel demonstrated a decrease in photocatalytic activity with an increase in calcination temperatures over 400-600°C [85]. The sol-gel process in association with surfactant-assisted templating has been used to synthesize several Ta_2O_5-based photocatalysts loaded with NiO cocatalyst [86]. Pt- or NiO loaded solid state reaction synthesized Cr-doped $Ba_2In_2O_5/In_2O_3$ composite semiconductor has been found to be a novel photocatalyst system with enhanced activity for water splitting under UV and visible light irradiation [87].

MCM-41 is mesoporus silicate, and generally considered an excellent catalyst support; its pore size can be systematically varied and photocatalytic substances readily incorporated. Liu and Wang prepared Zr-doped MCM-41 using a hydrothermal route achieving photocatalytic water decomposition about 2.5 times higher than conventional ZrO_2 catalysts [88]. Hydrothermally prepared Cr-doped MCM-41, sol gel loaded with 25 wt% TiO_2 has been found active under visible light irradiation [89]. Doping of metal cations and/or non-metal anions into oxide semiconductors can improve their visible light photocatalytic response with, of course, phase composition and specific surface areas affecting photocatalytic activity [29,30,49,61-63,85-92]. Recently hydrothermal approaches, good for preparing uniform nanosized particles, followed by ammonia nitridation yielded (S,N) codoped-titania as a visible light active photocatalyst [90]. Aita and co-workers used a solvothermal process to prepare N-doped titania in a hexamethylenetetramine-alcohol solution [91]. Yuan and co-workers used urea and titanium chloride as starting materials in preparing N-doped TiO_2 [92]. Recently deposition of Cu_2O quantum dots on TiO_2 nanoparticles was reported for water photoreduction under sacrificial conditions [93].

6.5 Design of Oxide Semiconductors

In the past several years noble metal loading, ion doping, composite metal-oxide semiconductors, and multi-component semiconductors have been meticulously designed, fabricated, and then investigated

for application to water splitting [45,46,49-59,63,65,82-89,93]. Liquid phase and gas phase syntheses routes, as described above, appear the most common synthesis approaches for production of these modified oxide semiconductor nanoparticle photocatalysts, some of which we now consider.

6.5.1 Metal Loaded Oxide Semiconductors
[6,7,9,10,12,15,17,45,94-107]

Various metals such as Cu, Ag, Au, Ni, Pd and Pt have been loaded on a variety of metal oxide semiconductors, but most of the work has focused on TiO_2. The Fermi level of metals is lower than that of TiO_2 so there is rapid transfer of photo-generated electrons from TiO_2 to the metal particles while the photo-generated holes remain in the TiO_2 valence band, resulting in efficient charge separation and consequently reduced possibility of electron-hole recombination. Although efficient charge separation by metal loading is partly able to reduce charge recombination, the occurrence of the thermodynamically favorable backward reaction inhibits generation of H_2 from pure water splitting.

Bamwenda et al. [45] employed Au and Pt loaded TiO_2 prepared by deposition-precipitation (DP), impregnation (IMP), photodeposition (PD), and colloidal mixing (CM) and compared their photocalytic activity for hydrogen production. Factors that affected H_2 production properties include synthesis methods, pretreatment conditions, metal loadings, and the oxide metal contact. The photocatlytic properties of nanoparticulate gold are found to be sensitive to the method of synthesis, with activity levels found in the following order: Au-TiO_2(FD) ≥ Au-TiO_2(DP) > Au-TiO_2(IMP) > Au-TiO_2(CM) and Pt-TiO_2(FD) > Au-TiO_2(DP) ≈ Au-TiO_2(IMP), respectively. Gold and platinum precursors calcined in air at 300°C were found to have the highest activity towards H_2 generation, followed by a decline in activity with increasing calcination temperature. The maximum H_2 yield observed for Pt-TiO_2 and Au-TiO_2 corresponded to metal loadings of, respectively, 0.3-1 wt.% and 1-2 wt.%. The roles of Au and Pt on TiO_2 seem to involve the attraction and trapping of photogenerated electrons, the reduction of

protons, and the formation and desorption of hydrogen. The higher overall activity of Pt samples is probably a result of the more effective trapping and pooling of photogenerated electrons by Pt and/or because platinum sites have a higher capability for the reduction reaction.

Hydrogen production from water by irradiating suspensions of Pt, Pd and Rh-loaded WO_3 in methylviologen (MV^{2+}) solution with visible light demonstrated efficiencies, in rank order, of Rh > Pt > Pd [95]. The conduction band level of WO_3 is not negative enough to reduce H^+ to H_2, but it readily reduces MV^{2+} which in turn helps reduce water. Simultaneous evolution of O_2 was observed since the valence band level of WO_3 is below the water oxidation level. The metal dopants act as sensitizers to increase the visible light absorption efficiency of the host semiconductors, i.e. photosensitization, and are also involved in the electron-transfer reactions such as capturing and transferring of conduction band electrons and/or valance band holes, thereby preventing electron-hole recombination and behaving as active sites for H^+ reduction.

Role of Carbonate Salts [97-100]

Despite a few successful experimental results Pt-loaded TiO_2 catalysts do not prevent the occurrence of backward reactions, with either reduced or no O_2 evolution from illuminated aqueous suspensions. Mill and Porter [96] identified photoadsorbed O_2 and $O_2^{\cdot -}$ over Pt-TiO_2 as agents interrupting the water splitting process. According to Arakawa and his coworkers [97], addition of sodium carbonate to the Pt-TiO_2 suspension can significantly improve stiochiometric decomposition of liquid water. Such systems [17, 98-100] introduce catalysts that facilitate the reaction as shown:

$$Na_2CO_3 \rightarrow 2Na^+ + CO_3^{2-} \quad (6.5.1)$$

$$CO_3^{2-} + H^+ \rightarrow HCO_3^- \quad (6.5.2)$$

$$HCO_3^- + h^+ \rightarrow HCO_3^{\cdot} \quad (6.5.3)$$

$$HCO_3^{\cdot} \rightarrow H^+ + CO_3^{\cdot -} \quad (6.5.4)$$

$$2CO_3^{\cdot -} \rightarrow C_2O_6^{2-} \quad (6.5.5)$$

$$C_2O_6^{2-} + 2h^+ \rightarrow O_2 + 2CO_2 \quad (6.5.6)$$

As seen in reaction (6.5.3) photogenerated holes are consumed, making electron-hole separation more effective as needed for efficient water splitting. The evolution of CO_2 and O_2 from reaction (6.5.6) can promote desorption of oxygen from the photocatalyst surface, inhibiting the formation of H_2O through the backward reaction of H_2 and O_2. The desorbed CO_2 dissolves in aqueous suspension, and is then converted to HCO_3^- to complete a cycle. The mechanism is still not fully understood, with the addition of the same amount of different carbonates, see **Table 6.2**, showing very different results [99]. Moreover, the amount of metal deposited in the host semiconductor is also a critical factor that determines the catalytic efficiency, see **Fig. 6.7**.

Table 6.2: Rate of photocatalytic production of H_2 and O_2 over a Pt/TiO_2 suspension with salts additives [99].

		Rate of evolution (μmol/h)[a]			
Additives	Amount (mol)	H_2	O_2	H_2/O_2	pH
None	-	1	0	-	7.9
Na_2CO_3	0.38	316	158	2.0	11.0
	0.76	568	287	2.0	11.0
	1.14	39	13	3.0	11.0
$NaHCO_3$	0.36	4	2	2.0	8.4
Li_2CO_3	0.06	5	1	5.0	10.8
K_2CO_3	0.38	5	1	5.0	11.5
	1.45	20	10	2.0	11.8
NaOH	0.76	5	0	-	13.3
NaCl	0.76	5	0	-	6.8
Na_2SO_4	0.38	4	0	-	5.5
Na_3PO_4	0.25	5	0	-	12.0

Catalyst: (0.3 wt% Pt/TiO_2); 0.3 g of catalyst suspended in 350 ml of water placed in an inner irradiator quartz cell. Irradiated with high-pressure mercury lamp (400 W).
[a] Rate at steady state.

With reference to **Fig. 6.7**, note there is no photocatalytic activity without Pt loading [99]; the rate of gas evolution increases with increasing Pt content reaching a maximum at 0.3 wt%. Other metals have shown similar trends in photocatalytic activity. Therefore, it is suggested that metal loading is one of the essential requirements for photocatalytic decomposition of liquid water. However the back reaction of evolved gas on the Pt particles increases with Pt loading. To suppress the backward reaction of H_2

and O_2 recombination the addition of an iodide anion (I^-) has shown significant effect [101]. It can preferentially adsorb on the Pt surface of an aqueous suspension of Pt-TiO_2, thereby forming an I_2 layer. The iodine layer in turn reduces the chances of a backward reaction occurring. However adding too much carbonate salt or iodide anion beyond an optimum level reduces the beneficial effects since the adsorbed species on the catalyst surface commonly decrease the light harvesting.

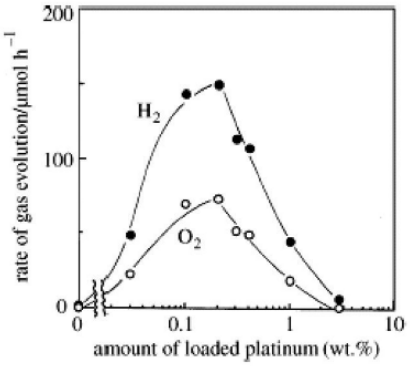

Fig. 6.7: Dependence of H_2 and O_2 evolution upon platinum loading. Water = 350 mL; Pt/TiO_2 = 0.3 g; Na_2CO_3 = 80 g. Reproduced with permission from Ref. [99].

Role of Mediators [45,102-107]

Rapid recombination of photogenerated electrons and holes can be controlled by electron donors (or hole scavengers) that irreversibly react with photo-generated holes leading to enhanced hole-electron separation. Since electrons are consumed during the photocatalyic process, for sustainable hydrogen production continuous electron-donating ability is required. Methanol, ethanol, lactic acid, formaldehyde, EDTA, CN^- have been widely used and proven to be effective electron donors for photocatalytic hydrogen production [45, 102-104]. For example, Wu and co-workers [102] reported the use of Cu-TiO_2 in aqueous methanol solutions. Nada et al. [104] employed different electron donors studying their effect on

hydrogen production; the rate of hydrogen production was found to decrease in the following order: EDTA > Methanol > ethanol > lactic acid. The hydrogen evolution rate over other metal oxide semiconductors are summarized in **Table 6.3.**

Table 6.3: Rate of H_2 evolution from aqueous methanol solution [17].

Catalyst	Rate of H_2 evolution (μmol/h)	Pt-catalyst	Rate of H_2 evolution (μmol/h)	Light abs. (< nm)
TiO_2	29	Pt/TiO_2	1166	413
Ta_2O_5	381	Pt/Ta_2O_5	2583	310
ZrO_2	971	Pt/ZrO_2	1546	248

Catalyst, 1.0 g;Water 350 mL; Pt 0.1 wt%, Light source: 400 W high-pressure Hg lamp; inner irradiation type quatz cell

Various pairs of inorganic ions such as IO_3^-/I^-, Fe^{3+}/Fe^{2+}, and Ce^{4+}/Ce^{3+} have been used as redox mediators to facilitate electron-hole separation in metal loaded oxide semiconductor photocatalysts [105-107]. Two different photocatalysts, Pt-TiO_2 (anatase) and TiO_2 (rutile), suspended in an aqueous solution of NaI were employed to produce H_2 and O_2 under, respectively, the mediation of I^- (electron donor) and IO_3^- (electron acceptor) [105]. The following steps are involved in a one-cell reaction in the presence of UV light.

At the Pt-TiO_2 (anatase) conduction band

$$6H^+ + 6e^- \rightarrow 3H_2 \qquad (6.5.7)$$

At Pt-TiO_2 (anatase) valence band

$$I^- + 6OH^- + 6h^+ \rightarrow IO_3^- + 3H_2O \qquad (6.5.8)$$

At the TiO_2 (rutile) conduction band

$$IO_3^- + 3H_2O + 6e^- \rightarrow I^- + 6OH^- \qquad (6.5.9)$$

At the TiO_2 (rutile) valance band

$$6OH^- + 6h^+ \rightarrow 3/2O_2 + 3H_2O \qquad (6.5.10)$$

For hydrogen production on the photocatalyst with the more negative conduction band, I^- can scavage holes [reaction (6.5.8)] thus conduction band electrons are available to reduce protons to H_2

molecules [reaction (6.5.7)]. For oxygen production on the photocatalyst with the more positive valence level, IO_3^- can react with electrons to form I^- [reaction (6.5.9)], hence the valance band holes are available to oxidize water forming oxygen [reaction (6.5.10)].

6.5.2 Mixed Metal-Oxide Semiconductors
[3,5,10,11,13-16,108,111-133]

Domen and co-workers, who observed the effect of NiO over $SrTiO_3$ powder for water splitting into H_2 and O_2 [5], later studied the mechanism and found that NiO acts as hydrogen evolution site while oxygen evolution occurs at $SrTiO_3$ [13]. A remarkable catalytic effect of RuO_2 on powdered TiO_2 for hydrogen evolution from an ethanol-water mixture has been observed by Sakata et al. [108]. To investigate the supporting effect of RuO_2 on TiO_2, experiments varying the amount of RuO_2 on a fixed amount of TiO_2 were carried out [108]; the rate for RuO_2/TiO_2, under illumination by a 500 W Xe lamp, was found to be 30 times higher than that for TiO_2 alone and sensitive to increasing amounts of RuO_2 reaching a maximum at 0.4×10^{-3} molar ratio of RuO_2/TiO_2, beyond which a decrease in performance was observed as the concentration of RuO_2 further increased. If present in small quantities these metal oxides act as electron pools (reducing sites) where H^+ is reduced to hydrogen. However when the concentration exceeds a critical limit they act as electron-hole recombination centers. One should, of course, use caution in deciding the amount of metal oxide co-catalyst to be loaded onto semiconductor particles, also chemical additives such as carbonate salt can significantly influence the water splitting reaction over mixed oxides.

Table 6.4: Photocatalytic decomposition of water over various semiconductor catalysts in Na_2CO_3 solution or pure water.

Semiconductor (Band gap, eV)	Loading (metal or metal oxide)	Rate of gas evolution (μmol/h)[a]				Ref.
		Na_2CO_3 solution		Pure Water		
		H_2	O_2	H_2	O_2	
TiO_2 (3.0)	None	Tr.	0	Tr.	0	17
	Pt (0.3 wt%)	78	38	2	0	
	RuO_2 (1.0 wt%)	34	17	Tr	0	
	NiO (1.0 wt%)	64	32	1	0	
Ta_2O_5 (4.0)	None	Tr.	0	Tr.	0	17
	Pt (0.3 wt%)	1	0	1	0	
	RuO_2 (1.0 wt%)	68	34	32	17	
	NiO (1.0 wt%)	153	79	190	99	
ZrO_2 (5.0)	None	142	75	72	36	17
	Pt (0.3 wt%)	53	23	Tr.	0	
	RuO_2 (1.0 wt%)	12	6	11	5	
	NiO (1.0 wt%)	43	22	129	70	
$SrTiO_3$ (3.0)	None	Tr.	0	Tr.	0	17
	Pt (0.1 wt%)	10	4	9	2	
	Rh (0.1 wt%)	48	14	20	4	
	NiO (1.0 wt%)	41	20	9	4	
$BaTi_4O_9$ (3.7)	Pt (0.1 wt%)	2	Tr.	Tr.	0	17
	RuO_2 (1.0 wt%)	36	18	30	13	
$K_2Ti_6O_{13}$	Pt (0.1 wt%)	63	17	Tr.	0	17
	RuO_2 (1.0 wt%)	49	24	11	1	
$K_4Nb_6O_7$	Pt (0.3 wt%)	451	217	Tr.	0	17
	RuO_2 (1.0 wt%)	60	28	403	197	
	NiO (1.0 wt%)	41	20	211	100	
$NaTaO_3$ (4.0)	None	-	-	160	86	111
	NiO (0.05 wt%)	-	-	2180	1100	111
	Au (0.3 wt%)	-	-	642	224	124
$LiTaO_3$ (4.7)	None	-	-	430	220	112
	NiO (0.1 wt%)	-	-	98	52	112
$KTaO_3$ (3.6)	None	-	-	29	13	112
	NiO (0.1 wt%)	-	-	7	3	112
	Au (0.3 wt%)	-	-	58	25	124
$Ba_2Ta_2O_6$ (4.1)	None	-	-	33	15	113
	NiO (0.5 wt%)	-	-	629	303	
$Sr_2Ta_2O_6$ (4.4)	None	-	-	140	66	114
	NiO (0.1 wt%)	-	-	960	490	
$Sr_2Ta_2O_7$ (4.6)	None	-	-	53	18	115
	NiO (0.15 wt%)	-	-	1000	480	115
$Sr_2Nb_2O_7$ (4.6)	None	-	-	5.9	0	115
	NiO (0.15 wt%)	-	-	10	3.2	115

Table 6.4 summarizes the water splitting properties of a number of mixed oxide semiconductors. In the presence of a co-catalyst such as NiO several highly active titanates, tantalates and niobates photocatalysts are reported for water splitting under UV light irradiation; $NiO/NaTaO_3$ is one of the most active catalysts, with a crystal structure of corner-shared MO_6 octahedra. In such compounds, e.g. $NaTaO_3$, the top of the valence band is primarily oxygen 2p non-bonding in character, while the conduction band arises from the π^* interaction between the transition metal t_{2g} orbitals (Ta_{5d}) and oxygen (O_{2p}). The band position changes with distortion and connection of the TaO_6 units. A study on luminescent properties has concluded that the closer the M-O-M bond angle is to 180° the more the excitation energy is localized [109]. Eng and co-workers [110] have carried out computational and experimental studies using orbital methods and UV-visible diffuse reflectance spectroscopy to quantitatively probe the relationships between composition, crystal structure and the electronic structure of oxides containing octahedrally coordinated d^0 transition metal ions such as Ti^{4+}, Nb^{5+}, and Ta^{5+}, primarily in perovskite and perovskite-related structures. For isostructural niobate, titanate and tantalate compounds the band gap increases as the effective electronegativity of the transition metal ion decreases. The effective electronegativity decreases in the following order: $Nb^{5+} \sim Ti^{4+} > Ta^{5+}$. Eng [110] also observed that the band gap is sensitive to changes in the conduction bandwidth, which can be maximized for structures possessing linear M–O–M bonds, such as the cubic perovskite structure. As this bond angle decreases the conduction band narrows and the band gap increases. This tendency indicates that photo-generated electron hole pairs can migrate relatively easily in the corner-shared framework of TaO_6 units. Niobate photocatalysts show differences in photocatalytic properties mainly due to conduction band energy levels, which are lower than in their Ta counterparts, and the degree of excitation energy delocalization.

Table 6.5: Effect of co-catalyst loaded $NaTaO_3$ photocatalysts on water splitting [112].

			Rate of gas evolution (μmol/h)	
Cocatalyst	Loading method	Amount (wt%)	H_2	O_2
None			166	93
CoO	IMP	0.1	42	21
NiO	IMP	0.1	1700	822
Ni	PD	0.16	219	110
CuO	IMP	0.14	72	38
RuO_2	IMP	0.2	147	78
Ag	IMP	0.2	38	12
Pt	PD	0.1	2.6	0

Catalyst: 1.0 g; Pure water: 350 mL; Light source: 400-W high-pressure mercury lamp; IMP stands for impregnation and PD stands for photodeposition.

The photocatalytic activities of the alkali tantalates, prepared by solid state reaction in the presence of excess alkali, lie in the following order: $KTaO_3 > NaTaO_3 > LiTaO_3$. As given in **Table 6.5**, NiO is found to be the most effective cocatalyst when loaded onto $NaTiO_3$. The conduction band levels of $NaTaO_3$ and NiO are, respectively, −1.06 eV and −0.96 eV. Therefore, the photogenerated electrons in the $NaTaO_3$ conduction band are able to transfer to the conduction band of NiO, which is an active site for hydrogen evolution and enhances charge separation. Pt is well known as an excellent co-catalyst for hydrogen evolution when combined with metal oxides. However Pt in combination with $NaTaO_3$ resulted in minimal hydrogen evolution, and no oxygen evolution due to the occurrence of a rapid reverse reaction on the Pt. Calcination temperatures have a strong influence on the $NiO/NaTiO_3$ activity due to the balance between activation by decomposition of $Ni(NO_3)_2$ and deactivation due to the destruction of the H^+ exchanged $NaTaO_3$ surface [111,112]. Similar behavior has been observed in other NiO loaded tantalates such as $BaTa_2O_6$, $SrTa_2O_6$, $Sr_2Ta_2O_7$ and $K_3Ta_3Si_2O_{13}$ with water splitting data summarized in **Table 6.4** [113-119].

$K_3M_3Si_2O_{13}$ (M =Ta and Nb) [119] possesses a unique pillared structure, in which three corner sharing MO_6 chains are bridged by ditetrahedral Si_2O_7 units. No photocatalytic activity for water splitting was observed from $K_3Nb_3Si_2O_{13}$, 4.1 eV bandgap, with or without cocatalyst addition. The M-O-M bond angles in

MO_6 chains of $K_3Ta_3Si_2O_{13}$ (bandgap = 3.9 eV) are 178° and 163° while those of $K_3Nb_3Si_2O_{13}$ are 174° and 167°. As described above, the distortion of the MO_6 octahedra strongly affect the energy structure of the photocatalysts. The 0.2 eV difference in bandgap is enough to dramatically alter the photocatalytic activities. $K_3Nb_3Si_2O_{13}$ showed no photoluminescence, ascribed to recombination between photo-generated electron - hole pairs at luminescence centers, with measurements at temperatures as low as 77K indicating that non-radiative transitions readily occur in $K_3Nb_3Si_2O_{13}$ leading to no photocatalytic activity.

Table 6.6 : Photocatalytic activities of mixed oxides prepared by SSR and PC methods.

Semiconductor	Preparation method (Cal. Temp.)[a]	Cocatalyst (wt%)	Surface area ($m^2\ g^{-1}$)	Rate of gas evolution (μmol/h)		Ref.
				H_2	O_2	
$Li_2Ti_2O_7$	SSR (1150°C)	Ni (1.0)	1.0	440	217	56
	PC (1050°C)	Ni (1.0)	1.0	960	478	
$Sr_2Nb_2O_7$ (3.9)	SSR (1100°C)	None	0.7	5.9	0	57
	SSR (1100°C)	NiO (0.15)	0.7	10	3.2	
	PC (900°C)	None	4.3	7.5	3.5	
	PC (900°C)	NiO (0.15)	4.3	94	46	
$Sr_2Ta_2O_7$ (4.5)	SSR (1100°C)	None	0.7	52	10	57
	SSR (1100°C)	NiO (0.15)	0.7	1000	480	
	PC (900°C)	None	4.3	2787	1347	
	PC (900°C)	NiO (0.15)	4.3	94	46	
	PC (800°C)	NiO(0.15)	10.4	3517	1733	
$K_2La_2Ti_3O_{10}$	SSR(900°C)	Ni (3 at.%)	4	1255	632	120
	PC (900°C)	Ni (3 at.%)	5	2186	1131	
$Sr_5Ta_4O_{15}$ (4.75)	PC (1000°C)	NiO (0.15)	2.99	1194	722	121
$Sr_4Ta_2O_9$ (4.81)	PC (1000°C)	NiO (0.15)	2.61	32	2	121
$Ba_5Ta_4O_{15}$ (3.90)	PC (800°C)	NiO (0.2)	-	7110	3621	122

[a]Calcination temperature. Catalyst: 0.7 g in 350 mL of water. Light source: 400-W high - pressure mercury lamp. PC stands for polymerizable complex while SSR stands for solid state reactions.

Table 6.6 summarizes photocatalytic water splitting properties of various mixed oxides prepared from two different processes, solid-state reaction (SSR) and solution based Pechini-type polymerizable complex routes [56,57,120-122]. $Ba_5Ta_4O_{15}$ prepared

by complex polymerization (sol-gel) shows the most remarkable photocatalytic activity of the layered perovskite type mixed oxide photocatalysts. $Ba_5Ta_4O_{15}$ precursor prepared with an excess amount of Ba and Ta, 25 at% above stoichiometric composition, produced 7110 and 3621 μmol/h H_2 and O_2, respectively, a rate nearly 3.5 times greater than that of the same compound fabricated with a precursor of stoichiometric composition (0.2 wt% NiO loading in each case) [122]. The topology of MO_6 (M = Ti, Ta, Nb) bonding in perovskite type compounds and its effect on the electronic structure of these systems is described by Eng and co-workers [110], who predicted that completely isolating the MO_6 octahedra (e.g., the ordered double perovskite structure) dramatically narrows the width of the conduction band leading to a significant increase in the band gap. These tantalates are composed of corner-sharing TaO_6 units. $Sr_4Ta_2O_9$ possesses the structure of the double perovskite and TaO_6 octahedra giving rise to an extremely narrow conduction band that cannot provide efficient carrier migration. The deviation of the M-O-M bond angle from 180° has been found to play a crucial role in photocatalyst performance. Thus despite the different symmetry and slightly different atomic layer arrangement in $Sr_4Ta_2O_9$ (cubic), $Sr_5Ta_4O_{15}$ (hexagonal) and $Sr_2Ta_2O_7$ (hexagonal), the trend in band gap energy should reflect differences in the width of the in conduction band [121], while inductive effects due to the presence of electropositive "spectator" cations (Li^+, Sr^{2+}, Ba^{2+}) tend to be small and can generally be neglected.

Abe and coworkers prepared R_3MO_7 and $R_2Ti_2O_7$ (R = Y, Gd, La; M = Nb, Ta) using the Pechini type complex polymerizable method [123]. These materials are composed of a network of corner-shared octahedral units of metal cations (TaO_6, NbO_6, or TiO_6); materials without such a network remain inactive. It is believed that the octahedral network increases the electron/hole mobility thereby enhancing photocatalytic activity. The photodeposition of gold nanoparticles on these photocatalysts (tantalates, niobates and titanates) containing shared MO_6 octahedra improve the overall water splitting reaction, see **Table 6.4** [124]. It appears that low doping levels of nanoscale gold particles minimizes backward reactions, enhances charge separation, and act as hydrogen evolution sites.

Visible Light Activity [125-133]

Most of the photocatalysts that we have discussed to this point have band gaps (> 3.0 eV) too large for responding to visible light. There are methods by which photocatalysts can be fabricated such that they will absorb visible light, including ion doping of wide band gap materials through hybridization of N 2p and O 2p orbitals as will be discussed in the next section. Another route is valence band formation using elements other than oxygen, for which single-phase oxide materials are of particular interest due to their intrinsic stability. Such materials include $BiVO_4$ [125], $AgNbO_3$ [126], Ag_3VO_4 [127], $Ca_2Bi_2O_4$ [128], $PbBi_2Nb_2O_9$ [129] and $InMO_4$ (M = Ta^{5+}; Nb^{5+}) [130]. The visible light responses of $BiVO_4$ and $AgNbO_3$ are attributable to a decrease in the band gaps due to valence band formation by not only O_{2p} but also $Bi^{3+}{}_{6s}$ and $Ag^{+}{}_{4d}$ orbitals. Visible light absorption in $PbBi_2Nb_2O_9$ is due to the transition from O_{2p} hybridized with Pb_{6s}/Bi_{6s} to Nb_{4d} and is reported to directly cleave water into H_2 and O_2. $InTaO_4$ and $InNbO_4$, with band gaps in the range 2.8 – 2.4 eV, are known to split water [130]. There are two kinds of octahedral, InO_6 and NbO_6 (or TaO_6), in a unit cell for both $InNbO_4$ and $InTaO_4$. The difference in unit cell volumes between TaO_6 and NbO_6 leads to a change in the lattice parameters slightly affecting their photocatalytic activity, mainly due to variation in the conduction band levels formed by Ta_{5d} TaO_6 and Nb_{4d} NbO_6.

Tai et al. has reported the preparation of $K_2La_2Ti_3O_{10}$ by a complex polymerization process followed by Au nanoparticle loading, either by impregnation (Au-i) or deposition-precipitation (Au-d) methods [131]. Au-i/$K_2La_2Ti_3O_{10}$ has shown superior water splitting properties in the UV and visible region compared to its counterpart Au-d/$K_2La_2Ti_3O_{10}$. The Au impregnation process resulted in better sample crystallinity than that prepared through Au-deposition-precipitation. Au-i/$K_2La_2Ti_3O_{10}$ is found more active for water splitting than Ni/$K_2La_2Ti_3O_{10}$ [120] under visible light illumination, but less active under UV. The high visible light activity of Au-i/$K_2La_2Ti_3O_{10}$ is attributed to plasma resonance absorption on the surface of the Au nanoparticles. This plasma resonance can polarize the electron distribution on the surface of the Au

nanoparticles, which increases the probability for electron transfer from gold to the $K_2La_2Ti_3O_{10}$ conduction band. In the case of Ni there is only absorption from the d–d transition in the visible region, which is not sufficient for transferring an electron from the Ni to the $K_2La_2Ti_3O_{10}$ surface [131].

Intercalation of nanosized Fe_2O_3 and TiO_2 particles within layered compounds such as $HNbWO_6$, $HTaWO_6$, $HTiNbO_5$ and $HTiTaO_5$ have been found to dramatically improve visible light photocatalytic activity [132,133], a behavior ascribed to more effective separation of photogenerated electrons - holes due to their rapid diffusion. Calcined samples of Fe-$HTiNbO_5$ and Fe-$HTiTaO_5$ are yellow in color, showing an absorption band edge at 600 nm. While their band gap energies are nearly 2.0 eV, the conduction band position is not negative enough to reduce water except in the presence of an electron acceptor ($AgNO_3$) [133].

6.5.3 Ion Doped Semiconductors

A common practice in modifying the band gap of a semiconductor is to include a small percentage of foreign elements into the regular crystal lattice. This is especially important in photocatalysis where high band gap oxide semiconductors can only be activated by light energy equal to or greater than their band gap energy, which generally falls in the UV region.

Cation Doping [49,58,62,87,89,134-149]

Doping of transition metal (V, Cr, Fe, Mo, Ru, Os, Re, V, Rh, etc.) and rare earth metal (La, Ce, Er, Pr, Gd, Nd, Sm, etc.) ions have been extensively used as a means of enhancing visible light-induced photocatalytic activities. Several experimental results confirm that metal ion doping expands the photo-response of TiO_2 into the visible region [134,135]. The metal ions incorporated into the TiO_2 lattice create new (impurity) energy levels within the TiO_2 band gap as shown in reactions (6.5.11) and (6.5.12), where M^{n+} represents dopant metal ions.

Charge pair generation

$$M^{n+} + h\nu \rightarrow M^{(n+1)+} + e^{-}(CB) \quad (6.5.11)$$

$$M^{n+} + h\nu \rightarrow M^{(n-1)+} + h^{+}(VB) \quad (6.5.12)$$

$e^{-}(CB)$ refers to a conduction band electron, or a trapped electron, and $h^{+}(VB)$ refers to a valence band hole, or a trapped hole; with respect to charge trapping:

Charge trapping

$$\text{Electron trap: } M^{n+} + e^{-}(CB) \rightarrow M^{(n-1)+} \quad (6.5.13)$$

$$\text{Hole trap: } M^{n+} + h^{+}(VB) \rightarrow M^{(n+1)+} \quad (6.5.14)$$

As shown in reactions (6.5.13) and (6.5.14), metal ion dopants influence the photoreactivity of metal oxides by acting as electron (or hole) traps thereby altering the e^{-}/h^{+}-pair recombination rate. The energy level of $M^{n+}/M^{(n-1)+}$ should be less negative than that of the TiO_2 conduction band (CB) edge, while the energy level of $M^{n+}/M^{(n+1)+}$ should be less positive than that of the TiO_2 valance band (VB) edge. Introduction of such energy levels within the band gap induces a red shift in the band gap transition, with enhanced visible light absorption due to charge transfer between a dopant energy level and the CB (or VB), or a d-d crystal field transition [134]. Since photocatalytic reactions are a surface phenomena, deep doping of metal ions are to be avoided for better charge injection or transfer properties. As we have repeatedly seen in various experiments the concentration of added metal ions affects the photocatalytic activity; above the optimum doping concentration photocatalytic activity decreases due to increased charge recombination [134].

Peng and co-workers [136] investigated the photocatalytic production of hydrogen using Be^{2+} doped TiO_2; the aqueous suspension contained 1.0 ml of ethanol (electron donor) and 0.33 ml of H_2PtCl_6. A 250 W high pressure Hg lamp was used as a light source. Two different methods, coprecipitation (CP) and impregnation (IMP) were chosen to prepare the required photocatalysts. **Figure 6.8(a)** shows the influence of doping method on hydrogen production by water splitting. Compared to the undoped TiO_2 both 1.25 at% Be^{2+}-TiO_2 and Be^{2+}-$P_{25}TiO_2$ (P_{25} is commercially available from Degussa AG, Germany. Surface area = 45 m^2g^{-1}, 70% anatase and 30% rutile,

purity >99.5%) prepared by IMP show a 75% increase in hydrogen production. In dramatic contrast, 1.25 at% Be^{2+}-TiO_2 and Be^{2+}-$P_{25}TiO_2$ prepared by coprecipitation (CP) shows a 36% decrease in the photocatalytic hydrogen production compared to pure TiO_2. Low activity in the CP samples can be attributed to the presence of the Be^{2+} ions within the bulk TiO_2 lattice hence the trapped photoexcited electron cannot easily migrate to the surface. The IMP Be^{2+}-TiO_2 doped ions are located on or near the TiO_2 surface, providing ready access of the photoexcited electrons to the reaction interface. As anticipated the amount of dopant further influences the hydrogen production rate, **Fig. 6.8b**. The deposition of Be^{2+} onto TiO_2 particles can produce oxygen vacancies, and lead to formation of a space charge layer facilitating separation of the photo-generated electron-hole pairs. Also Ti-O-Be formed via Be^{2+} entering the TiO_2 surface could promote charge transfer due to the difference in electro-negativity of Ti and Be, resulting in an increase in photocatalytic activity. As anticipated, a continual increase in Be^{2+} doping concentration beyond some optimal point shows degradation in photocatalytic properties. The origin for this behavior can vary with the material system being studied; in the case of Be^{2+} on a TiO_2 surface it appears to increase the number of recombination centers [136]. This observation is similar to one observed by Choi et al with other metal ion dopants [134].

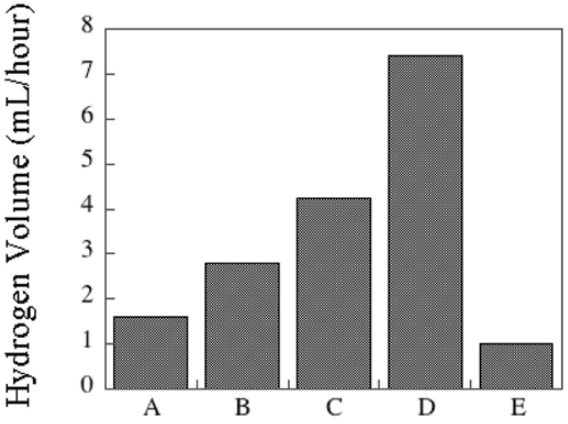

Fig. 6.8a: Photocatalytic hydrogen production from samples doped via coprecipitation (CP) and impregnation (IMP). **(a)** TiO_2; **(b)** 1.25 at% Be^{2+}-TiO_2-IMP; **(c)** P_{25}-TiO_2; **(d)** 1.25 at% Be^{2+}-P_{25}-TiO_2-IMP; **(e)** 1.25 at% Be^{2+}-P_{25}-TiO_2-CP.

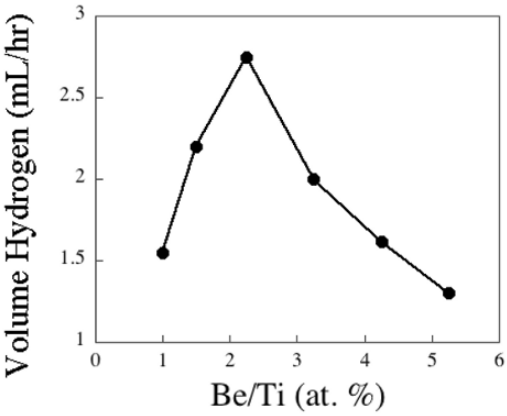

Fig. 6.8b: Photocatalytic hydrogen production as a function of dopant (Be^{2+}) content [136].

Hameed et al. [137] investigated the photolysis properties of transition metal ion doped WO_3 (bandgap = 2.6 eV). As seen in **Fig. 6.3**, the conduction band level of WO_3 is lower than $E°(H_2/H_2O)$ hence WO_3 suspended in water cannot reduce protons to hydrogen molecules. Doping with metal ions such as Fe, Co, Ni, Cu and Zn allows formation of the corresponding oxides on the WO_3 surface. Since the conduction band levels of Fe, Co, Ni and Cu oxides are higher than $E°(H_2/H_2O)$, the conduction band electrons can readily reduce protons [137]. In the case of Mg-doping (10 wt%), the conduction band edge position shifted about 1.82 V higher than $E°(H_2/H_2O)$ thereby thermodynamically allowing H^+ ion to reduce to hydrogen, however the valence band edge shifted about 0.25 V higher than $E°(H_2O/O_2)$ inhibiting water oxidation [49].

Mixed metal oxides having spinel ($MM'O_4$), perovskite ($MM'O_3$) and layered perovskite ($M_2M_2'O_7$) structures, where M and M′ represent two different metals, have been doped with various transition metal ions to tailor their band gap towards the visible spectrum. Direct splitting of water under visible light irradiation with Ni doped indium-tantalum-oxide, $In_{(1-x)}Ni_xTaO_4$ (x = 0-0.2) has been reported by Zou and co-workers [138]. This catalyst was prepared as follows: pre-dried solid In_2O_3, Ta_2O_5 and NiO powders were heated at 1100°C to prepare $InNiTaO_4$. 1.0 wt% Ni particles were impregnated on the surface of $InNiTaO_4$ followed by

calcination at 350°C and reduction in H_2 atmosphere (200 torr) at 773°C, then treated in O_2 atmosphere (100 torr) at 200°C. The rates of hydrogen and oxygen evolution for $In_{0.90}Ni_{0.10}TaO_4$ are found to be about 16.6 and 8.3 μmol/h ($\lambda > 420$ nm), respectively, and the quantum yield at 402 nm approximately 0.66%. The Ni doping reduced the band gap from 2.6 eV (undoped) to 2.3 eV (doped), attributed to internal d-d transitions in a partly filled d shell.

The introduction of a new valence band or electron donor energy level appears an effective, or at least reasonable, strategy for developing visible light photocatalysts. These photocatalysts and their photocatalytic activities are summarized in **Table 6.7** [139-144]. Rh doped $Pt/SrTiO_3$ shows visible light response ($\lambda > 420$ nm) due to the transition from the electron donor level formed by the Rh^{3+} ion to the conduction band composed of the Ti_{3d} orbitals of $SrTiO_3$ [139]. Similarly, $Pt/SrTiO_3$ codoped with a combination of either antimony, or tantalum and chromium, involves energy gap level transitions from the donor energy level formed by Cr^{3+} to the conduction band of $SrTiO_3$, resulting in visible light absorption. Charge balance is maintained by codoping of Sb^{5+} and Ta^{5+}, resulting in the suppression of the formation of Cr^{6+} ions and oxygen defects within the lattice [140,141].

Table 6.7: Visible-light-driven ($\lambda > 420$ nm) photocatalysts for H_2 and/or O_2 from aqueous solution in the presence of sacrificial reagents.

Semiconductors:doped	Band gap (eV)	Sacrificial reagent	Rate of gas evolution (μmol/h)		Ref.
			H_2	O_2	
$Pt/SrTiO_3$: Rh	2.3	CH_3OH	117	-	139
TiO_2:Cr, Sb	2.5	$AgNO_3$	-	42	140
$Pt/SrTiO_3$:Cr, Sb	2.5	CH_3OH	78	-	140
$Pt/SrTiO_3$:Cr, Ta	2.3	CH_3OH	70	-	141
$Pt/La_2Ti_2O_7$:Cr	2.2	CH_3OH	15	-	142
$Pt/La_2Ti_2O_7$:Fe	2.6	CH_3OH	10	-	142
$InTaO_4$: Ni	2.6	$CH_3OH/AgNO_3$	3.1	1.1	143
TiO_2: Ni, Ta	2.6	$CH_3OH/AgNO_3$	-	7.6	144
$SrTiO_3$:Ni, Ta	2.8	$CH_3OH/AgNO_3$	2.4	0.5	144

Reactions were carried out in presence of sacrificial agents. O_2 evolution: aqueous silver nitrate solution. H_2 evolution: aqueous methanol solution.
Light source: 300-W Xe lamp

Lanthanum doping of NiO-loaded $NaTaO_3$, NiO(0.2 wt%)/$NaTaO_3$:La(2%) resulted in a 9x increase in H_2 and O_2 evolution rates to 19.8 and 9.7 mmol/h, respectively, under UV light illumination [145]; the maximum apparent quantum yield reported was 56% at 270 nm. Electron microscope observations revealed the particle size of the NiO/$NaTaO_3$:La photocatalyst lies in the range of 100-700 nm, smaller the undoped NiO/$NaTaO_3$ crystals of 2-3 μm. The small particle size, excellent crystallinity, as well as creation of a surface topology comprised of 'nano-steps' due to the La doping appears to help reduce unwanted electron-hole recombination. Loading of ultrafine NiO particles on the step edges helps separate the H_2 and O_2 evolution sites avoiding back reaction during water splitting, **Fig. 6.9**. Evidence suggests that H_2 evolution proceeds on the ultrafine NiO particles, while O_2 evolution occurs at grooves on the step-like structures of the La:$NaTaO_3$.

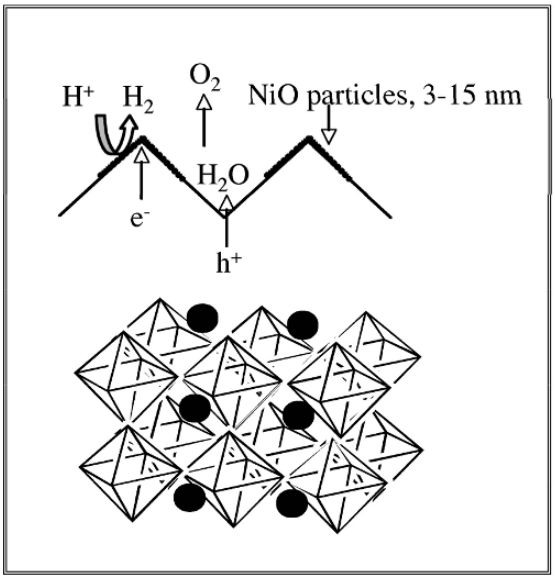

Fig. 6.9: Mechanism of water splitting on surface of NiO/$NaTaO_3$:La photocatalyst [145].

IrO_2 has also been used as a co-catalyst with $NaTaO_3$:La [146]; it was found that IrO_2 is involved in the formation of sites active for O_2 evolution. Other metal oxides such as γ-Bi_2O_3 and

Fe_2O_3, doped with various metal ions have been applied to photocatalytic hydrogen production in the presence of methyl viologen (MV^{2+}) that serves as an electron donor [147]. The photocatalytic hydrogen production efficiency of γ-Bi_2O_3 has shown an activity doping dependence of: $Pd^{2+} > Ru^{3+} > Co^{2+} > Ni^{2+} > Fe^{3+} > Cr^{4+}$ > undoped γ-Bi_2O_3. Formation of Schottky-type barrier at the metal dopant - γ-Bi_2O_3 junction leads to more effective charge separation due to the enhanced internal electric field. The smaller the barrier height, given by the difference between the work function of the dopant and electron affinity of γ-Bi_2O_3, the greater the electron flow from γ-Bi_2O_3 to the metal, thus allowing the metal ions to behave as cathodes.

Z-scheme Construction [148-149]

A combined system involving two photoexcitation processes is called a Z-scheme, due to the similarity of the intrinsic process to photosynthesis. For example, a combination of Pt-WO_3 and Pt-$SrTiO_3$ (Cr-Ta doped) were found effective in utilizing visible light for H_2 and O_2 production in a NaI solution [148]. Over an extended duration H_2 and O_2 evolution under monochromatic light (420.7 nm, 57 mW) were measured at 0.21 μmol/h of H_2 and 0.11 μmol/h of O_2; the estimated quantum efficiency was 0.1%. Similarly Fe^{3+}/Fe^{2+} and Ce^{4+}/Ce^{3+} pairs are also effective for hydrogen production by water splitting [149]. Pt/$SrTiO_3$:Rh works as a photocatalyst for H_2 production using Fe^{2+} ions, while $BiVO_4$ acts as a photocatalyst for O_2 production using Fe^{3+} ion, see **Fig. 6.10.**

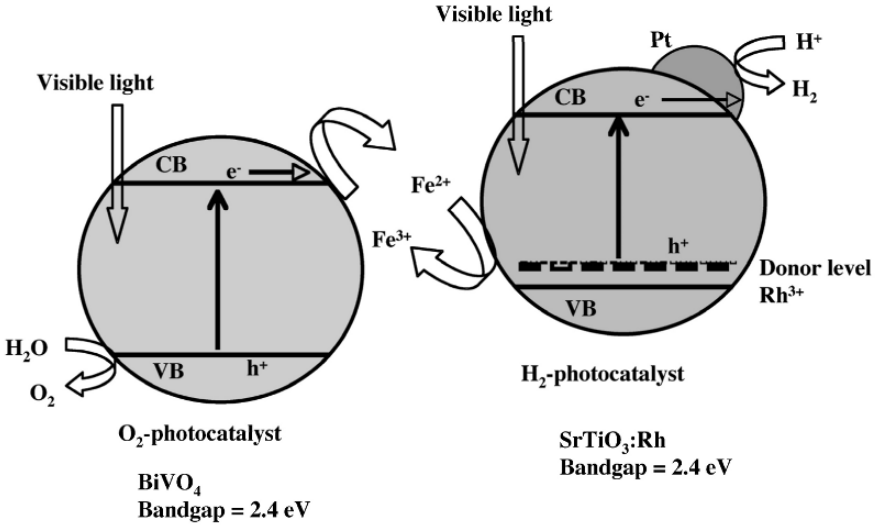

Fig. 6.10: Z-scheme system for water splitting by a two-photon process with visible light response [149].

Anion Doping [29,30,63,90-92,150-159]

Doping of anions such as N, F, C, and S in metal oxide or mixed metal oxides can shift the photoresponse into the visible region [150-159] while showing little tendency to form recombination centers [63, 90-92,155-158]. Asahi and co-workers studied the substitutional doping of C, N, F, P and S for O in anatase TiO_2 [150]. It was found that mixing of N p states with O 2p states could shift the valence band edge upwards, narrowing the band gap of TiO_2. Incorporation of S into the TiO_2 lattice of is a bit difficult due to the large ionic radius, while C, N and P doping has resulted in reduced mobility of the photo-generated charges.

Synthesis of nanoparticulate N-doped TiO_2 can be carried out by a variety of methods, including the heating of titanium hydroxide and urea [151], nitriding of anatase TiO_2 with alkyl ammonium salts [152], and heating TiO_2 powder in presence of NH_3/Ar gas at 550°C [153]. Anion doping results in an upward shift in the valence band energy without affecting the conduction band energy level, resulting in a narrower band gap. Since the valence

band level of TiO_2 is far more positive than the oxygen evolution energy level, anion doped TiO_2 suffers from the limited availability of holes for water oxidation. Incorporation of sulpher atoms into the TiO_2 lattice in the form of S^{4+} can be carried out by annealing TiS_2 at 600°C in oxygen [154], and by mixing titanium isopropoxide with thiourea in ethanol [155]. It was found that mixing of S 3p states with the valance band of TiO_2 results in band gap narrowing and thereby improved visible light photocatalytic activities. Co-doped metal oxides such as $Sr_{1-x}La_xTiO_{3-x}N_x$ ($SrTiO_3$:La:N) and rutile TiO_2:La_2O_3:S synthesized by, respectively, sol-gel and hydrothermal processes have been used for photodecomposition of organic compounds under visible light [156,157].

Lee et al. [158] reported the use of N-doped $Sr_2Nb_2O_7$ for water splitting under visible light irradiation. $Sr_2Nb_2O_{7-x}N_x$ (x = 1.47~2.828) catalysts were synthesized from a $Sr_2Nb_2O_7$ precursor by ammonia nitridation at temperatures ranging from 700°C to 1000°C. The photocatalysts prepared at 800°C showed maximum catalytic activity, while above this temperature it gradually decreased. The photocatalyst structure, layered perovskite, appears to be the most important parameter determining the photocatalytic activity. It has been demonstrated that materials of layered-type structure have higher catalytic activity for water splitting than unlayered materials of the same composition. Excess N-doping facilitates the collapse of the layered structure of the parent oxide, $Sr_2Nb_2O_7$, turning it into unlayered $SrNbO_2N$, a behavior that possibly explains the reduction in photocatalytic activity for samples processed at temperatures above 800°C.

As seen from the band model for $Sr_2Nb_2O_7$ (**Fig. 6.11**), the states at the top of the valence band come from O 2p orbitals, while states at the conduction band minimum are predominantly from Nb_{4d}. The main difference observable in the nitrogen-doped oxide is that the major contribution at the valence band comes from N 2p. Density of states (DOS) studies suggest that N substitution doping gives rise to band gap narrowing by mixing of N 2p with O 2p states near the top of the valence band. This band gap narrowing enables the material to shift the optical absorption into visible light range [159].

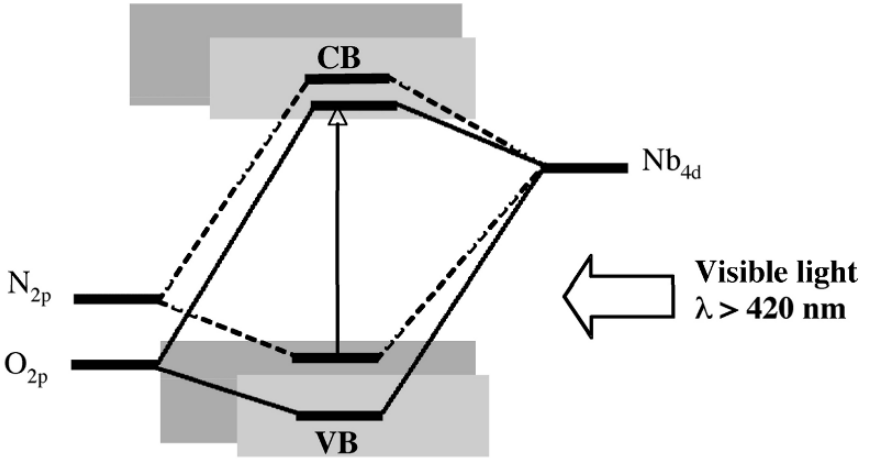

Fig. 6.11: A band model of N-doped $Sr_2Nb_2O_7$ shows mixing of N_{2p} with O_{2p} states near the top of the valence band leading to band gap narrowing and visible light activity.

6.5.4 Dye-Sensitized Oxide Semiconductors [160-165]

Considerable efforts have been made in the area of dye-sensitized photocatalytic hydrogen production [160-165]. In this process dye molecules absorb light with the transfer of an electron from the ground state to an excited state. The excited electron passes from the dye to the conduction band of an appropriate metal oxide (usually TiO_2). The conduction band electron can then be transferred to metal particles loaded on the surface to initiate water reduction. To regenerate the dye, sustaining the reaction, sacrificial reagents such as EDTA can be added to the solution [163,165]. Fast electron injection and slow backward reaction make dye-sensitized semiconductors feasible for hydrogen production [161-163].

Abe and co-workers [160] used xanthene dye on Pt/TiO_2 for hydrogen production from aqueous triethanolamine solution (TEOA) under visible light irradiation. In order to make a stable dye-sensitized photocatalyst a silane-coupling reagent (γ-aminopropyl triethoxysilane) was used to replace the carboxyl group of the xanthene dye with an amino group. Dhanlakshmi et al. [164] carried out a similar experiment using $[Ru(dcpy)_2(dpq)]^{2+}$. With or without Pt loading of TiO_2, no significant changes in the rate of

hydrogen production have been seen suggesting that only dye molecules adsorbed on the TiO_2 surface are sufficiently effective in injecting electrons into TiO_2 for water reduction. The effects of various dyes such as eosin blue, rose Bengal, rhodamine B, and $[Ru(bpy)_3]^{2+}$ on photocatalytic hydrogen production by SnO_2, with or without sacrificial agents, have been studied by Gurunathan and co-workers [165]; to date no significant results with reference to hydrogen production have been reported so far.

6.6 Conclusions and Future Prospects

During the past several decades aqueous suspensions of semiconductor particles have been appraised for direct photocatalytic water splitting under UV and visible light irradiation, where each particle behaves as its own electrochemical cell. It has been observed that photogenerated charge separation, prevention of backward reactions, and utilization of a large fraction of the incident solar energy are the essential requirements for achieving high photoconversion efficiencies. The addition of carbonate salts or other electron mediators to the water have shown enhanced hydrogen production by preventing backward reactions. Enhanced hydrogen production has also been shown by the addition of electron donors or hole scavengers that irreversibly react with valence band holes to inhibit charge recombination, while to attain sustainable hydrogen production electron donors must be continuously added.

The most successful of the oxide semiconductors synthesized for aqueous suspension H_2 production by solar light are composed of two or more components. Various syntheses procedures such as loading and/or doping of metal or metal oxide particles on the surface of base photocatalysts have been successfully employed for water photosplitting. Cation doping can lead to an increase in charge carrier recombination centers, introduced by the localized d-states of the dopants deep within the TiO_2 bandgap. Anion doping is found effective in terms of band gap narrowing for harnessing visible light energy; the related impurity energy levels, while near the valence band edge, do not act as charge carriers. Most of the reactions carried out using doped oxide semiconductors are half-reactions that produce either hydrogen or oxygen in the presence of sacrificial

agents. These agents scavenge electrons or holes in an irreversible manner making the process unsustainable. Use of a metal and nonmetal co-doped oxide semiconductor system appears a logical extension in the design of a robust photocatalytic system. A variety of perovskite type mixed-oxide nanoparticle photocatalysts have shown significant performances, but stability and phase purity remain a challenge to accomplish overall water splitting.

A concerted effort is needed to screen potentially useful oxide semiconductor systems and find ways to design nanostructure architectures of oxide semiconductors, metals/metal oxides as cocatalysts and/or other light harvesting assemblies. These developments require collaboration with suitable theoretical modeling for a better understanding of the hydrogen production mechanism in order to achieve low-cost and environmental friendly direct water-splitting for hydrogen production.

References

1. Fujishima A, Honda K (1972) Electrochemical photolysis of water at a semiconductor electrode. Nature 238:37–38
2. Schrauzer GN, Guth TD (1977) Photolysis of water and photoreduction of nitrogen on titanium oxide. J Am Chem Soc 99:7189–7193
3. Kawai T, Sakata T (1980) Photocatalytic decomposition of gaseous water. Chem Phys Lett 72:87–89
4. Van Damme H, Hall WK (1979) On the photoassisted decomposition of water at the gas-solid interface on TiO_2. J Am Chem Soc 101:4373–4374
5. Domen K, Naito S, Soma M, Onishi T, Tamaru K (1980) Photocatalytic decomposition of water vapor on a NiO-$SrTiO_3$ catalyst. Chem Commun 543–544
6. Sato S, White JM (1980) Photodecomposition of water over Pt/TiO_2 catalysts. Chem Phys Lett 72:83–86
7. Wagner FT, Somerjai GA (1980) Photocatalytic and Photoelectrochemical hydrogen production on strontium titanate single crystals. J Am Chem Soc 102:5494–5502

8. Wagner FT, Somerjai GA (1980) Photocatalytic production from water on Pt-free $SrTiO_3$ in aqueous alkaline solution. Nature 285:559–560
9. Sato S, White JM (1981) Photocatalytic water decomposition and water-gas shift reactions over NaOH coated, platinized TiO_2. J Catal 69:128–139
10. Duonghong D, Borgarello E, Grätzel M (1981) Dynamics of light induced water cleavage in colloidal system. J Am Chem Soc 103:4685–4690
11. Domen K, Naito S, Onishi T, Tamaru K (1982) Photocatalytic decomposition of liquid water on a NiO-$SrTiO_3$ catalyst. Chem Phys Lett 92:433–434
12. Lehn JM, Sauvage JP, Ziessel R, Hilaire L (1982) Water photolysis by UV irradiation of rhodium loaded strontium titanate catalysts. Relation between catalytic activity and the nature of the deposit from combined photolysis and ESCA studies. Israel J Chem 22:168–172
13. Domen K, Kudo A, Onishi T (1986) Mechanism of photocatalytic decomposition of water into H_2 and O_2 over NiO-$SrTiO_3$. J Catal 102:92–98
14. Kudo A, Domen K, Maurya K, Aika K, Onishi T (1988) Photocatalytic decomposition of water over NiO-$K_4Nb_6O_{17}$ catalysts. J Catal 111:67–76
15. Inoue Y, Kubokawa Y, sato K (1991) Photocatalytic activity of alkali-metal titanates combined with Ru in the decomposition of water. J Phys Chem 95:4059–4063
16. Inoue Y, Asai Y, sato K (1994) Photocatalysts with tunnel structures for decomposition of water. J Chem Soc Faraday Trans 90:797–802
17. Sayama K, Arakawa H (1994) Effect of Na_2CO_3 addition on photocatalytic decomposition of liquid water over various semiconductor catalysts. J Photochem Photobiol A Chem 77:243–247
18. Sayama K, Arakawa H (2000) Oxide semiconductor materials for solar light energy Utilization. Res Chem Intermed 26:145–152

19. Baba R, Nakabayashi S, Fujishima A, Honda K (1985) Investigation of the mechanism of hydrogen evolution during photocatalytic water decomposition on metal-loaded semiconductor powders J Phys Chem 89:1902–1905
20. Aspnes DE, Heller A (1983) Photoelectrochemical hydrogen evolution and water- photolyzing semiconductor suspensions: Properties of platinum group metal catalyst emiconductor contacts in air and in hydrogen. J Phys Chem 87:4919–4929
21. Bard AJ, Fox MA (1995) Artificial photosynthesis: Solar splitting of water to hydrogen and oxygen. Acc Chem Res 28:141–145
22. Ashok Kumar M (1998) An overview of semiconductor particulate system for photoproduction of hydrogen. Int J Hydrogen Energy 23:427–438
23. Kudo A, Kato H, Tsuji I (2004) Strategies for the development of visible-light-driven photocatalysts for water-splitting. Chem Lett 33, 1534-1539
24. Takata T, Tanaka A, Hara M, Kondo JN, Domen K (1998) Recent progress of photocatalysts for overall water splitting. Catal Today 44:17–26
25. Kamat PV (1993) Photochemistry on nonreactive and reactive (semiconductor) surfaces. Chem Rev 93: 267–300
26. Thompson TL, Yates J T (2005) TiO2-based photocatalysis: Surface defects, oxygen and charge transfer. Top Catal 35:197–210
27. Hagfeldt A, Gratzel M (1995) Light-Induced Redox Reactions in Nanocrystalline Systems Chem Rev 95:49-68
28. Hara M, Kondo T, komoda M, Ikeda S, Shinohara K, Tanaka A, Kondo JN, Domen K (1998) Cu_2O as a photocatalyst for overall water splitting under visible light irradiation. Chem Commun 357–358
29. Morikawa T, Asahi R, Ohwaki T, Aoki K, Taga, Y (2001) Bandgap narrowing of titanium dioxide by nitrogen doping. Jpn J Appl Phys Part 2-Lett 40:L561–L563
30. Wang H, Lewis JP (2006) Second-generation photocatalytic materials: anion-doped TiO_2. J Phys-C, 18:421–434

31. A. Kudo (2003) Photocatalyst materials for water splitting. Catal Surv Asia 7:31–38
32. Ni M, Leung MKH, Leung DYC, Sumathy K (2007) A review and recent development in photocatalytic water splitting using TiO_2 for hydrogen production. Renewable and Sustainable Energy Reviews 11:401–425
33. Kudo A (2006) Development of photocatalyst materials for water splitting. Int J Hygrogen Energy 31:197–202
34. Murray CB, Kagan CR (2000) Synthesis and Characterization of monodispersed nanocystals and closed-packed nanocrystals assemblies. Annu. Rev Mater Sci 30, 545–610
35. Cushing BL, Kolesnichenko VL, O'Connor CJ (2004) Recent advances in the liquid-phase syntheses of inorganic nanoparticles. Chem Rev 104:3893–3946.
36. H. Hahn (1997) Gas phase synthesis of nanocrytalline materials. Nanostuct Mater 9:3–12
37. Swihart MT (2003) Vapor synthesis of nanoparticles. Curr Opin Colloid Interf Sci 8:127–133
38. Wang Y, Ma C, Sun X, Li H (2002) Preparation of nanocrystalline metal oxide powders with the surfactant mediated method. Inorg Chem Commun 5:51–755
39. Zhang Z, Guo L, Wang W (2001) Synthesis and characterization of antimony oxide nanoparticles. J Mater Res 16:803-805
40. Haruta M, Tsubota S, Kobayashi T, Kageyama H, Genet MJ, Delmon B (1993) Low temperature oxidation of CO over gold supported TiO_2, α-Fe_2O_3 and Co_3O_4. J Catal 144:175–192
41. Liu ZL, Liu YZ, Yao KL, Ding ZH, Tao J, Wang X (2002) Synthesis and magnetic properties of Fe_3O_4 nanoparticles. J Mater Synth Process 10:83–87
42. Tang ZX, Sorenson CM, Klabunde KJ, Hajipanayis GC (1991) Size dependent Curie temperature in nanoscale $MnFe_2O_4$. Phy Rev Lett 67:3602–3605

43. You X, Chen, F, Zhang J, Anpo M (2005) A novel deposition-precipitation method for preparation of Ag-loaded TiO_2. Catal Lett 102:247–250
44. Zanella R, Giogio S, Shin CH, Henry CR Louis C (2004) Characterization and reactivity in CO oxidation of gold nanoparticles supported on TiO_2 prepared by deposition-preparation with NaOH and Urea. J Catal 222:257–267
45. Bamwenda GR, Tsubota S, Nakamura T, Haruta M (1995) Photoassisted hydrogen production from a water-ethanol system: a comparison of activities of Au-TiO_2 and Pt-TiO_2. J Photochem Photobio A 89:177–189
46. Abe T, Suzuki, E, Nagoshi, K, Miyashita K, Kaneko M (1999) Electron source in photoinduced hydrogen production on Pt supported TiO_2 particles. J Phys Chem 103:1119-1123
47. Chan SC, Barteau MA (2005) Preparation of highly uniform Ag/TiO_2 and Au/TiO_2 supported nanoparticles catalyst by photodeposition. Langmuir 23:5588-5595
48. Borgarello E, Serpone N, Emo G, Harris R, Pelizzetti E, Minero C (1986) Light-induced reduction of rhodium (III) and palladium (II) on titanium dioxide dispersions and the selective photochemical separation and recovery of gold (III), platinum (IV) and rhodium (III) in chloride media. Inorg Chem 25:4499–4503
49. Hwang DW, Kim J, Park TJ, Lee JS (2002) Mg-doped WO_3 as a novel photocatayst for visible light-induced water splitting. Catal Lett 80:53-57
50. Galinksa A, Walendziewski J (2005) Photocatalytic water splitting over Pt-TiO_2 in the presence of sacrificial reagents. Energy & Fuels 19:1143-1147
51. Cao Y, Hsu JC, Hong ZS, Deng JF, Fan KN (2002) Characterization of high-surface-area zirconia aerogel synthesized from alcohothermal and supercritical fluid drying techniques.Catal Lett 81:107–112
52. Bischoff BL, Anderson MA (1995) Peptization process in the sol-gel preparation of anatase TiO_2. Chem Mater 7:1772–1778

53. Chang YS, Chang YH, Chen IG, Chen GJ, Chai YL (2002) Synthesis and characterization of zinc titanate nano-crystal powders by sol-gel technique. J Cryst Growth 243:319–326
54. Xuewen W, Zhiyong Z, Shuixian Z (2001) Preparation of nano-crystalline $SrTiO_3$ powder in sol-gel process. Mater Sci Engg B 86:29–33
55. Kohno M, Ogura S, Inoue Y (1996) Preparation of $BaTi_4O_9$ by a sol-gel method and its photocatalytic activity for water decomposition. J Mater Chem 6:1921–1924
56. Kim HG, Hwang DW, Bae SB, Jung JH, Lee JS (2003) Photocatalytic water splitting over $La_2Ti_2O_7$ synthesized by the polymerizable complex method. Catal Lett 91:193–198
57. Yoshino M, Kakihana M, Cho WS, Kato H, Kudo A (2002) Polymerizable complex synthesis of pure $Sr_2Nb_xTa_{2-x}O_7$ solid solutions with high photocatalytic activities for water decomposition into H_2 and O_2. Chem Mater 14:3369–3376
58. Yener DO, Giesche H (2001) Synthesis or pure and manganese-, nickel- and zinc-doped ferrite particles in water-in-oil microemulsions. J Am Ceram Soc 84:1987–1995
59. Kapoor MP, Inagaki S, Yoshida H (2005) Novel zirconium-titanium phosphates mesoporous materials for hydrogen production by photoinduced water splitting. 109:9231–9238
60. Oguri Y, Riman RE, Bowen HK (1988) Processing of anatase prepared from hydrothermally treated alkoxy derived hydrous titania. J Mater Sci 23:2897-2904
61. Chen H, Ma J, Zhao Z, Qi L (1995) Hydrothermal preparation of uniform nanosize rutile and anatase particle. Chem Mater 7:663–671
62. Jeon S, Braun PV (2003) Hydrothermal synthesis of Er-doped luminescent TiO_2 nanoparticles. Chem Mater 15:1256–1263
63. Lou H, Takata T, Lee Y, Zhao J, Domen K, Yan Y (2004) Photocatalytic activity enhancing for titanium dioxide by codoping with chlorine and bromine. Chem Mater 16:846–849

64. Yan M, Cheng F, Zhang J, Anpo M (2005) Preparation of controllable crystalline titania and study on the photocatalytic properties. J Phys Chem B 109:8673–8678
65. Ikeda S, Fuboki M, Takahara YK, Matsumura M (2006) Photocatalytic activity of hydrothermally synthesized tantalates pyrochlores for overall water splitting. Appl Catal A 300:186–190
66. Hulteen JC, Martin CR (1997) A general template base method for the preparation of nanomaterials. J Mater Chem 7:1075-1087
67. Shchukin DG, Schattka JH, Antonietti M, Curasu RA (2003) Photocatalytic properties of porous metal oxide networks formed by nanoparticles infiltration in a polymer gel template. J Phys Chem B 107:952-957
68. Lensveld DJ, Mesu JG, van Dillen AJ, de Jong KP (2001) Synthesis and characterization of MCM-41 supported nickel oxide catalysts. Microporous Mesoporous Mat 44-45:401–407
69. Valdés-Solís T, Marbán G, Fuertes AB (2005) Preparation of nanosized perovskites and spinels through a silica xerogel template route. Chem Mater 17:1919-1922
70. Nasibulin AG, Richard O, Kauppinen EI, Brown DP, Jokiniemi JK, Altman IS (2002) Nanoparticle synthesis by copper(II) acetylacetonate vapor decomposition in the presence of oxygen. Aerosol Sci Technol 36:899–911
71. Schmechel R, Kennedy M, von Seggern H, winkler H, Kolbe M, Fischer RA, Xaomao L, Benker A, Winterer M, Hahn H (2001) Luminescence properties of nanocrystalline Y_2O_3:Eu^{3+} in different host materials. J Appl Phys 89: 1679–1686
72. Ahonen PP, Joutsensaari J, Richard O (2001) Mobility size development and the crystallization path during aerosol decomposition synthesis of TiO_2 particles. J Aerosol Sci 32:615–630
73. Johannessen T, Jenson JR, Mosleh M, Johansen J, Quaade U, Livbjerg H (2002) Flame synthesis of nanoparticles: Application in catalysis and product/process engineering. Chem Eng Res Des 82:1444-1452

74. Mädler L, Kammler HK, Mueller R, Pratsinis SE (2002). Controlled synthesis of nanostructured particles by flame spray pyrolysis. J Aerosol Sci 33:369 –388
75. Flagan RC, Lunden MM (2004) Particle structure control in nanoparticle synthesis from the vapor phase. 204:113-124
76. Ohno T (2002) Morphology of composite nanoparticles of immiscible binary systems prepared by gas-evaporation technique and subsequent vapor condensation. J Nanoparticle Res 4:255 –260
77. Iwasaki M, Iwasaki Y, Tada H, Ito S (2004) One-pot process for anodic oxide films of titanium with high photocatalytic activity. Mater Trans 45: 1607–1612
78. Harano A, Shimada K, Okubo T, Sadakata M. (2002) Crystal phases of TiO_2 ultrafine particles prepared by laser ablation of solid rods. J Nanoparticle Res 4:215 –219
79. Iwabuchi A, Choo CK, Tanaka K Titania Nanoparticles Prepared with Pulsed Laser Ablation of Rutile Single Crystals in Water J Phys Chem B 108:10863–10871
80. Guimaraes JL, Abbate M, Betim SB, Alves MCM (2003) Preparation and characterization of TiO_2 and V_2O_5 nanoparticles produced by ball-milling J Alloys & Compounds 352:16–20
81. Damonte LC, Zelis LAM, Soucase BM, Fenollosa MAH Nanoparticles of ZnO obtained by mechanical milling. Powder Tech 148: 15–19
82. Shimizu K, Itoh S, Hatamachi T, Kodama T, Sato M, Toda K (2005) Photocatalytic water splitting on Ni-intercalated Ruddlesden-Popper type $H_2La_{2/3}Ta_2O_7$. Chem Mater 17:5161–5166
83. Ebina Y, Sasaki T, Harada M, Watanabe M (2002) Restacked perovskite nanosheets and their Pt-loaded materials as photocatalysts Chem Mater 14: 4390-4395
84. Ebina Y, Sakai N, Sasaki T (2005) Photocatalyst of Lamellar Aggregates of RuOx Loaded Perovskite Nanosheets for Overall J Phys Chem B 109:17212-17216
85. Cheng P, Li W, Zhou T, Jin Y, Gu M (2004) Physical and photocatalytic properties of zinc ferrite doped titania under

visible light irradiation. J Photochem Photobiol A: Chem 168:97–101
86. Sreethawong T, Ngamsinlapasathian S, Suzuki Y, Yoshikawa S (2005) Nanocrystalline mesoporus Ta_2-based photocatalysts prepapred by surfactant-assisted templating sol-gel process photocatalytic H_2 evolution. J Mol Catal A:Chem 235:1–11
87. Wang D, Zou Z, Ye J (2005) Phtotcatalytic water splitting with the Cr-doped $Ba_2In_2O_5/In_2O_3$ composite oxide semiconductors. Chem Mater 17:3255-3261
88. Liu SH, Wang HP (2002) Photocatalytic generation of hydrogen on Zr-MCM-41. Int J Hydrogen Energy 27:859–862
89. Sun B, Reddy EP, Smirniotis PG (2005) Effects of the Cr^{6+} concentration in Cr-incorporated TiO_2-loaded MCM-41 catalysts for visible light photocatalysis. Appl Catal B: Environmental 57:139–149
90. Liu H, Gao L (2004) (Sulfur, Nitrogen)-codoped rutile-titanium oxide as a visible-light-activated photocatalyst. J Am Ceram Soc 87:1582–1584
91. Aita Y, Komatsu M, Yin S, Sato T (2004) Phase-compositional control and visible light photocatalytic activity of nitrogen-doped titania via solvothermal process. J Solid state Chem 177:3235–3238.
92. Yuan J, Chen M, Shi J, Shangguan W (2006) Preparation and photocatalytic hydrogen evolution of N-doped TiO_2 from urea and titanium tetrachloride. Int J Hydrogen Energy 31:1326–1331
93. Senevirathna MKI, Pitigala PKDDP, Tennakone K (2005) Water photoreduction with Cu_2O quantum dots on TiO_2 nano-particles. J Photochem Photobiol A: Chem 171:257–259
94. Tabata S, Nishida H, Masaki Y, Tabata T (1995) Stoichiometetric photochemical decomposition of pure water in Pt/TiO_2 aqueous suspension system. Cat Lett 34:245–249
95. Marathamuthu P, Ashokkumar M (1989) Hydrogen production with visible light using metal loaded WO_3 and

MV^{2+} in aqueous medium. Int J Hydrogen Energy 14:275–277
96. Mill A, Porter G (1982) Photosensitized dissociation of water using dispersed suspensions of n-type semiconductors. J Chem Soc Faraday Trans.1 78:3659–3669
97. Sayama K, Arakawa H (1992) Significant effect of carbonate addition on stoichiometric photodecomposition of liquid water into hydrogen and oxygen from platinum-titanium(IV) oxide suspension. J Chem Soc Chem Commun 150–152
98. Sayama K, Arakawa H (1994) Effect of carbonate addition on the photocatalytic decomposition of liquid water over a ZrO_2 catalyst. J Photochem Photobiol A: Chem 94:67–76
99. Sayama K, Arakawa H (1997) Effect of carbonate salt addition on the photocatalytic decomposition of liquid water over Pt-TiO_2 catalysts. J Chem Soc Faraday Trans 93:1647–1654
100. Arakawa H, Sayama K (2000) Solar hydrogen production: significant effect of Na_2CO_3 addition on water splitting using simple oxide semiconductor photocatalysts. Catal Surv Jpn 4:75–80
101. Abe R, Sayama K, Arakawa H (2003) Significant effect of iodide addition on water splitting into H_2 and O_2 over Pt-loaded TiO_2 photocatalyst: suppression of backward reaction. Chem Phys Lett 371:360–364
102. Wu NL, Lee MS (2004) Enhanced TiO_2 photocatalysis by Cu in hydrogen production from aqueous methanol solution. Int J Hydrogen Energy 29:1601–1605
103. Lee SG, Lee SW, Lee HI (2001) Photocatalytic production of hydrogen from aqueous solution containing CN^- as a hole scavengers.Appl Catal A:Gen 207:173–181
104. Nada AA, Barakat MH, Hameed HA, Mohamad NR, Veziroglu TN (2005) Studies on the photocatalytic hydrogen production using suspended modified TiO_2 photocatalysts. Int J Hydrogen Energy 30:987–991
105. Abe R, Sayama K, Domen K, Arakawa H (2001) A new type of water splitting system composed of two different TiO_2

photocatalysts (anatase, rutile) and a IO_3^-/I^- shuttle redox mediator. Chem Phys Lett 344:339–344
106. Bamwenda GR, Arakawa H (2001) The photoinduced evolution of O_2 and H_2 from a WO_3 aqueous suspension in presence of Ce^{4+}/Ce^{3+}. Sol Energy Mater Sol Cells 70:1–14
107. Lee K, Nam WS, Han GY (2004) Photocatalytic water splitting in alkaline aqueous solution using redox mediator 1: parameter study. Int J Hydrogen Energy 29:1343–1347
108. Sakata T, Hashimoto K, Kawai T (1984) Catalytic properties of ruthenium oxide on n-type semiconductors under illumination. J Phys Chem 88:5214–5221
109. Srivastava AM, Ackerman JF (1997) On the luminescence of $Ba_5M_4O_{15}$ (M = Ta^{5+} and Nb^{5+}). J Solid State Chem 134, 187–191
110. Eng HW, Barnes PW, Auer BM, Woodword PM (2003) Investigation of the electronic structure of d^0 transition metal oxides belonging to the perovskite family. J Solid State Chem 175:94–109
111. Kato H, Kudo A (1999) Highly efficient decomposition of pure water over $NaTaO_3$ photocatalysts. Catal Lett 58:153–155
112. Kato H, Kudo A (2001) Water splitting into H_2 and O_2 on Alkali tantalate photocatalysts $ATaO_3$. J Phys ChemB 105:4285–4292
113. Kato H, Kudo A (1999) A new tantalate photocatalyst for water decomposition into H_2 and O_2. Chem Phys Lett 295: 487–492
114. Kato H, Kudo A (1999) Photocatalytic decomposition of pure water into H_2 and O_2 over $SrTa_2O_6$ prepared by flux method. Chem Lett 1207–1209
115. Kudo A, Kato H, Nakagawa S (2000) Water splitting into H_2 and O_2 on New $Sr_2M_2O_7$ (M = Nb and Ta) photocatalysts with layered perovskite structures: Factor affecting the photocatalytic activity. J Phys Chem B 104:571–575
116. A. Kudo A, Okutomi H, Kato H (2000)Photocatalytic water splitting into H_2 and O_2 over $K_2LnTa_5O_{15}$. Chem Lett 1212–1213.

117. Yamashita Y, Tada M, Kahihana M, Osada M, Yoshida K (2002) Synthesis of RuO_2-loaded $BaTi_2O_{2n+1}$ (n = 1, 2 and 5) using a polymerizable complex method and its photocatalytic activity for the decomposition of water. J Mater Chem 12:1782–1786
118. Miseki Y, Kato H, Kudo A (2005) Warer splitting into H_2 and O_2 over $Cs_2Nb_4O_{11}$. Chem Lett 54–55
119. Kato H, Kudo A (2003) Photocatalytic water splitting into H_2 and O_2 over various tantalate photocatalysts. Catal Today 78:561–569
120. Ikeda S, Hara M, Kondo JN, Domen K (1998) Preparation of $K_2La_2Ti_3O_{10}$ by polymerized complex method and photocatalytic decomposition of water. Chem Mater 10: 72-77
121. Yoshioka K, Petrykin V, Kakihana M, Kato H, Kudo A (2005) The relationship between photocatalytic activity and crystal structure in Strontium tantalates. J Catal 232:102–107
122. Otsuka H, Kim K, Kouzu A, Takimoto I, Fujimori H, Sakata Y, Imamura H, Matsumoto T, Toda K (2005) Photocatalytic performance of $Ba_5Ta_4O_{15}$ to decomposition of H_2O into H_2 and O_2. Chem Lett 822–823
123. Abe R, Higashi M, Sayama K, Abe Y, Sugihara H (2006) Photocatalytic activity of R_3MO_7 and $R_2Ti_2O_7$ (R = Y, Gd, La; M = Nb, Ta) for water splitting into H_2 and O_2. J Phys Chem B 110:2219–2226
124. Iwase H, Kato H, Kudo A (2006) Nanosized gold particles as an efficient cocatalyst for photocatalytic overall water splitting. Catal Lett 108:6–9
125. Kudo A, Omri K, Kato H (1999) A novel aqueous process for preparation of crystal form-controlled and highly crystalline $BiVO_4$ powder from layered vanadates at room temperature and its photocatalytic and photophysical properties. J Am Chem Soc 121:11459–11467
126. Kato H, Kobayashi H, Kudo A (2002) Role of Ag^+ in the band structures and photocatalytic properties of $AgMO_3$ (M = Nb and Ta) with the perovskite structure. J Phys Chem B 106:12441–12447

127. Konta R, Kato H, Kobayashi H, Kudo A (2003) Photophysical properties and photocatalytic activities under visible light irradiation of silver vanadates. Phys Chem Chem Phys 5:3061–3065
128. Tang J, Zou J, Ye J (2004) Efficient photocatalytic decomposition of organic contaminants over $Ca_2Bi_2O_4$ under visible-light irradiation. Angew Chem Int Ed 43:4463–4466
129. Kim HG, Hwang DW, Lee JS (2004) An undoped, single-phase oxide photocatalyst working under visible light. J Am Chem Soc 126:8912–8913
130. Zou Z, Ye J, Arakawa H (2003) Photocatalytic water splitting into H_2 and or O_2 under UV and visible light irradiation with a semiconductor catalyst. Int J Hydrogen Energy 28:663–669
131. Tai YW, Chen JS, Yang CC, Wan BJ (2004) Preparation of nano-gold on $K_2La_2Ti_3O_{10}$ for producing hydrogen from photo-catalytic water splitting. Catal Today 97:95–101
132. Wu J, Uchida S, Fujishito Y, Yin S, Sato T (1999) Synthesis and photocatalytic properties of $HNbWO_6/TiO_2$ and $HNbWO_6/Fe_2O_3$ nanocomposite. J Photochem Photobiol A: Chem 128:129–133
133. Jang JS, Kim HG, Reddy VR, Bae SW, Ji SM, Lee JS (2005) Photocatalytic water splitting over iron oxide nanoparticles intercalated in $HTiNb(Ta)O_5$ layered compounds. J Catal 231:213–222
134. Choi WY, Termin A, Hoffman MR (1994) The role of metal ion dopants in quantum-sized TiO_2: Correlation between photoreactivity and charge carrier reaction dynamics. J Phys Chem 98:13669–13679
135. Xu AW, Gao Y, Liu HQ (2002) The preparation, characterization and their photocatalytic activities of rare-earth doped TiO_2 nanoparticles. J Catal 207:151–157
136. Peng S, Li Y, Xiang F, Lu G, Li S (2004) Effects of Be^{2+} doping on its photocatalytic activity. Chem Phys Lett 398:235–239
137. Hameed A, Gondal MA, Yamini ZH (2004) Effects of transition metal doping on photocatalytic activity of WO_3 for

water splitting under laser illumination: role of 3d-orbitals. Catal Commun 5:715–719
138. Zou Z, Ye J, Sayama K, Arakawa H (2001) Direct splitting of water under visible light irradiation with an oxide semiconductor photocatalyst. Nature 414:625–627
139. Konta R, Ishii T, Kato H, Kudo A (2004) Photocatalytic activities of noble metal ion doped $SrTiO_3$ under visible light irradiation. J Phys Chem 108:8992–8995
140. Kato H, Kudo A (2002) Photocatalytic activities of noble metal ion doped $SrTiO_3$ under visible light irradiation. J Phys Chem B 106:5029–5034
141. Ishii T, Kato H, Kudo A (2004) H_2 evolution from an aqueous methanol solution on $SrTiO_3$ photocatalysts codoped with chromium and tantalum ion under visible light irradiation. J Photochem Photobiol A: Chem 163:181–186
142. Hwang DW, Kim HG, Lee JS, Kim J, Li W, Oh SH (2005) Photocatalytic hydrogen production from water over M-doped $La_2Ti_2O_7$ (M = Cr, Fe) under visible light irradiation ($\lambda > 420$ nm). J Phys Chem B 109:2093–2102
143. Zou Z, Ye J, Sayama K, Arakawa H (2002) Photocatalytic hydrogen and oxygen formation under visible light irradiation with M-doped $InTaO_4$ (M = Mn, Fe, Co, Ni, Cu) photocatalysts. J Photochem Photobiol A:Chem 148:65–9
144. Niishiro R, Kato H, Kudo A (2005) Nickel and either tantalum or niobium co-doped TiO_2 and $SrTiO_3$ photocatalysts with visible-light response for H_2 or O_2 evolution from aqueous solution. Phys Chem Chem Phys 7:2241–2245
145. Kato H, Asakura K, Kudo A (2003) Highly efficient water splitting into H_2 and O_2 over lanthanum-doped $NaTaO_3$ photocatalysts with high crystallinity and surface nanostructure. J Am Chem Soc 125:3082–3089
146. Iwase A, Kato H, Kudo A (2005) A novel photodeposition method in the presence of nitrate ions for loading of an iridium oxide cocatalyst for water splitting. Chem Lett 34, 946–947

147. Gurunathan K (2004). Photocatalytic hydrogen production using transition metal ions-doped γ-Bi2O3 semiconductor particles, Int J Hydrogen Energy 29:933–940
148. Sayama K, Masuka K, Abe R, Abe Y, Arakawa H (2001) Stiochiometric water splitting into H_2 and O_2 using a mixture of two different photocatalysts and an IO_3^-/I^- shuttle redox mediator under visible light irradiation. Chem Commun 2416–2417
149. Kato H, Hori M, Konta R, Shimodaira Y, Kudo A (2004) Construction of Z-scheme type heterogeneous photocatalysis systems for water splitting into H_2 and O_2 under visible light irradiation Chem Lett 33:1348–1349
150. Asahi R, Morikawa T, Ohwaki T, Aoki K, Taga Y (2001) Visible light photocatalysis in nitrogen-doped titanium oxide. Science 293:269–271
151. Kobayakawa K, Murakami K, Sato Y (2004) Visible-light active N-doped TiO_2 prepared by heating of titanium hydroxide and urea. J Photochem Photobiol A:Chem 170:177–179
152. Gole JL, Stout JD, Burda C, Lou YB, Chen XB (2004) Highly efficient formation of visible light tunable $TiO_{1-x}N_x$ photocatalysts and their transformation at nanoscale. J Phys Chem B 108:1230–1240
153. Mrowetz M, Balcerski W, Colussi AJ, Hoffmann MR (2004). Oxidative power of N-doped TiO_2 photocatalysts under visible light illumination J Phys Chem B 108:17269–17273
154. Umebayashi T, Yamaki T, Itoh H, Asai K (2002) Band gap narrowing of titanium oxide by sulphur doping. Appl Phys Lett 81:454-456
155. Ohno T, Akiyoshi M, Umebayashi T, Asai K, Mitsui T, Matsumura M (2002) Preparation of S-doped TiO_2 photocatalysts and their photocatalytic activites under visible light. Appl Catal A: Gen 265:115-121
156. Miyauchi M, Takashio M, Tobimatsu H (2004) Photocatalytic activity of $SrTiO_3$ codoped with nitrogen and lanthanum under visible light illumination. Langmuir 20:232–236

157. Liu HY, Gao L (2004) Codoped rutile TiO_2 as a new photocatalyst for visible light irradiation. Chem Lett 33:730–731
158. Ji SM, Borse PH, Kim HG, Hwang DW, Jang JS, Bae SW, Lee JS (2005) Photocatalytic hydrogen production from water-methanol mixtures using N-doped $Sr_2Nb_2O_7$ under visible light irradiation; effect of catalyst structures. Phys Chem Chem Phys 7:1315–1321
159. Lee JS (2006) Photocatalytic water splitting under visible light with particulate semiconductor catalysts. Catal Surv Asia 9:217–227
160. Abe R, Hara K, Sayama K, Domen K, Arakawa H (2000) Steady hydrogen evolution from water on Eosin-Y-fixed TiO_2 photocatalyst using a silane coupling reagent under visible light irradiation. J Photochem Photobiol A: Chem 137:63–69
161. Abe R, Sayama K, Arakawa H (2002) Efficient hydrogen evolution from aqueous mixture of I^- and acetonitrile using a merocyanine dye-sensitized Pt/TiO_2 photocatalyst under visible light irradiation. Chem Phys Lett 362:441–444
162. Abe R, Sayama K, Arakawa H (2004) Dye-sensitized photocatalysts for efficient hydrogen production from aqueous I^- solution under visible light irradiation. J Photochem Photobiol A: Chem 166:115–122
163. Bae E, Choi W (2006) Effect of the anchoring group (carboxylate vs phosphonate) in Ru-complex-sensitized TiO2 on hydrogen production under visible light. Source. J Phys Chem B 30:14792–14799
164. Dhanlakshmi KB, Latha S, Anandan S, Maruthamuthu P (2001) Dye-sensitized hydrogen evolution from water Int J Hydrogen Energy 26:669–674
165. Gurunathan K, Maruthamuthu P, Shastri VC (1997) Photocatalytic hydrogen production by dye-sensitized Pt/SnO_2 and $Pt/SnO_2/RuO_2$ in aqueous methyl viologen solution. Int J Hydrogen Energy 22:57–62